Downloaded from https://academic.oup.com/mnras/article/542/2/8233647 by library@ist.ac.at user on 03 September 2025



Advance Access publication 2025 August 13

Can supermassive stars form in protogalaxies due to internal Lyman-Werner feedback?

James Sullivan[®], 1^{*} Zoltán Haiman [®], 1,2,3 Mihir Kulkarni [®]4,5 and Eli Visbal [®]4

Accepted 2025 July 28. Received 2025 July 28; in original form 2025 January 31

ABSTRACT

Population III stars are possible precursors to early supermassive black holes (BHs). The presence of soft UV Lyman-Werner (LW) background radiation can suppress Population III star formation in minihaloes and allow them to form in pristine atomiccooling haloes. In the absence of molecular hydrogen (H₂) cooling, atomic-cooling haloes enable rapid collapse with suppressed fragmentation. High background LW fluxes from preceding star-formation have been proposed to dissociate H₂. This flux can be supplemented by LW radiation from one or more Population III star(s) in the same halo, reducing the necessary background level. Here, we consider atomic-cooling haloes in which multiple protostellar cores form close to one another nearly simultaneously. We assess whether the first star's LW radiation can dissociate nearby H₂, enabling rapid accretion on to a nearby protostellar core, and the prompt formation of a second, supermassive star (SMS) from warm, atomically-cooled gas. We use a set of hydrodynamical simulations with the code ENZO, with identical LW backgrounds centred on a halo with two adjacent collapsing gas clumps. When an additional large local LW flux is introduced, we observe immediate reductions in both the accretion rates and the stellar masses that form within these clumps. While the LW flux reduces the H₂ fraction and increases the gas temperature, the halo core's potential well is too shallow to promptly heat the gas to $\geq 1000 \, \mathrm{K}$ and increase the second protostar's accretion rate. We conclude that this internal LW feedback scenario is unlikely to facilitate SMS or massive BH seed formation.

Key words: stars: black holes – stars: massive – stars: Population III – galaxies: star-formation.

1 INTRODUCTION

Supermassive black holes (SMBHs) are found at the centre of nearly all nearby galaxies (Kormendy & Ho 2013) and play a major role in their evolution. However, the formation and evolution of these SMBHs is still shrouded in uncertainty. There are several proposed routes to explain the presence of SMBHs as massive as $10^{8-9} \,\mathrm{M}_{\odot}$ as early as $z \sim 6$ (Fan et al. 2006; Venemans et al. 2015; Wu et al. 2015; Bañados et al. 2018; Inayoshi, Visbal & Haiman 2020; Wang et al. 2021; Fan, Bañados & Simcoe 2023; Bosman 2024). The most common pathways can be divided into the following categories: a 'normal' massive Population III (hereafter Pop III) star ($\sim 10^{1-2} \, \mathrm{M}_{\odot}$) forms and its remnant BH accretes large amounts of mass, possibly at hyper-Eddington rates, to form a SMBH; an intermediate-mass BH $(\sim 10^{3-4} \,\mathrm{M}_{\odot})$ forms and grows to a SMBH through accretion and/or mergers; or finally, a massive primordial star ($\sim 10^{5-6} \,\mathrm{M}_{\odot}$) forms, collapses promptly into a massive BH, and then grows by steady accretion (Inayoshi et al. 2020; Volonteri, Habouzit & Colpi 2021).

Several cosmological simulations have found inefficient growth of stellar-mass BH seeds, making the first route disfavoured (Alvarez,

* E-mail: jms2561@columbia.edu

Wise & Abel 2009; Milosavljević, Couch & Bromm 2009; Smith et al. 2018; Spinoso et al. 2022). However, rare periods of high, tumultuous accretion could provide a pathway to large masses for a small subset of these stellar-mass seeds. If the direction of these accretion flows is uncorrelated, the BH will have lower spin rates and radiative efficiency, consequently increasing growth (Zubovas & King 2021).

Forming SMBHs from intermediate-mass seeds requires runaway collisions and is therefore limited to dense stellar clusters. However, studies demonstrate difficulties growing BHs larger than $10^{3-4} \, \mathrm{M}_{\odot}$ (Portegies Zwart et al. 2004; Omukai, Schneider & Haiman 2008; Devecchi & Volonteri 2009; Katz, Sijacki & Haehnelt 2015; González et al. 2021; Rizzuto et al. 2021). Supermassive stars (SMSs) have consequently been proposed as a route to form SMBHs, avoiding the need for high collision rates or super-Eddington accretion (Begelman & Rees 1978; Rees 1978; Begelman, Volonteri & Rees 2006; Begelman, Rossi & Armitage 2008; Latif, Schleicher & Hartwig 2016; Woods et al. 2019). In this paper, we focus on this latter scenario.

Simulations predict that Pop III stars form in 10⁵–10⁶ M_☉ minihaloes (Haiman, Thoul & Loeb 1996; Tegmark et al. 1997; Machacek, Bryan & Abel 2001; Abel, Bryan & Norman 2002; Bromm, Coppi & Larson 2002; Yoshida et al. 2003; Hirano et al.

¹Department of Astronomy, Columbia University, 550 West 120th Street, New York, NY 10027, USA

²Department of Physics, Columbia University, 550 West 120th Street, New York, NY 10027, USA

³Institute of Science and Technology Austria (ISTA), Am Campus 1, A-3400 Klosterneuburg, Austria

⁴Department of Physics and Astronomy and Ritter Astrophysical Research Center, University of Toledo, 2801 W. Bancroft Street, Toledo, OH 43606, USA

⁵Institut für Astrophysik, Georg-August Universität Göttingen, Friedrich-Hund-Platz 1, D-37077 Göttingen, Germany

2014; Greif 2015; Kulkarni, Visbal & Bryan 2021; Klessen & Glover 2023). These first stars form in metal-free regions and are composed of hydrogen, helium, and trace amounts of lithium (Yoshida, Hosokawa & Omukai 2012; Bromm 2013; Klessen 2019). These pristine haloes have virial temperatures less than the atomic-cooling threshold, $\sim 10^4$ K, so they cool via molecular hydrogen (H₂) rovibrational transition lines (Bromm & Loeb 2003; Bromm & Yoshida 2011). However, supernovae quickly enrich the gas with metals. This is in part due to the short stellar lifespans of massive Pop III stars, which are on the order of a few Myr. The higher efficiency of metal cooling leads to transition to lower-mass Population II (Pop II) stars.

Pop III stars produce large numbers of Lyman–Werner (LW) photons, ranging from 11.2 to 13.6 eV and above, throughout their lifetime. These contribute to an early background LW radiation as the star formation density increases. This radiation can drastically affect future star formation. In pristine haloes, the LW radiation can dissociate H_2 and prevent cooling by its rovibrational transitions. Thus in regions with strong LW radiation, Pop III star formation will be suppressed in minihaloes with virial temperatures $T_{\rm vir} \lesssim 10^4$ K, which rely on H_2 to cool (Haiman et al. 1996; Tegmark et al. 1997; Haiman, Abel & Rees 2000; Machacek et al. 2001; O'Shea & Norman 2007; Wise & Abel 2007).

Atomic-cooling haloes (ACH) are thus a promising potential location for massive Pop III star formation. These haloes have total (dark matter + gas) masses of $10^{7\text{--}8}\,M_{\odot}$, corresponding to virial temperatures of $T_{\rm vir} \approx 10^4 \, \rm K$ at redshifts 10–20 (Omukai 2001; Prieto, Jimenez & Haiman 2013; Becerra et al. 2014; Regan et al. 2020). In the absence of LW radiation, collapsing gas experiences rapid H₂ cooling and fragments. This favors the formation of multiple 'normal' Pop III stars at the Jeans mass corresponding to the temperature at which cooling becomes inefficient (see review by Inayoshi et al. 2020). However, with intense LW radiation, H₂ is dissociated and the temperature remains roughly isothermal at $T \simeq 10^4$ K for much of the collapse. With the corresponding large gas accretion rate, a supermassive star can form with a mass as high as $10^{4-6} \, \mathrm{M}_{\odot}$ (Bromm et al. 2002; Wise, Turk & Abel 2008; Regan & Haehnelt 2009a, b). These SMSs become unstable and collapse into similarly massive BHs, becoming potential SMBH seeds. Recent studies (Hosokawa, Omukai & Yorke 2012; Hosokawa et al. 2013; Woods et al. 2017; Haemmerlé et al. 2018; Nandal et al. 2023) have set this critical accretion rate between 0.01–0.04 M_☉ yr⁻¹. 2D simulations by Sakurai et al. (2016) showed that brief periods of slower accretion are allowed and will not prevent SMS formation, as long as the duration of such an episode does not exceed $10^3 [M_*/500 \,\mathrm{M}_{\odot}]^{\frac{1}{2}} \,\mathrm{yr}$. This therefore also requires a gas supply on the order of $10^5 \,\mathrm{M}_{\odot}$ to feed the growing protostar. In the absence of either/both of this sustained and rapid accretion, the protostar will settle on to the main sequence at lower masses. Protostars accreting below the critical rate will self-limit due to UV feedback and form 'normal' massive stars between $\sim 10^{2-3} \ \mathrm{M}_{\odot}$. Stars that accrete above the critical accretion rate but are limited by the available gas mass can form very massive stars (VMSs) between $\sim 10^{3-4}~M_{\odot}$. These VMSs do not undergo a GR instability but nevertheless directly collapse at the end of their lives and leave BH remnants (referred to as Type III collapsars in Heger et al. 2003).

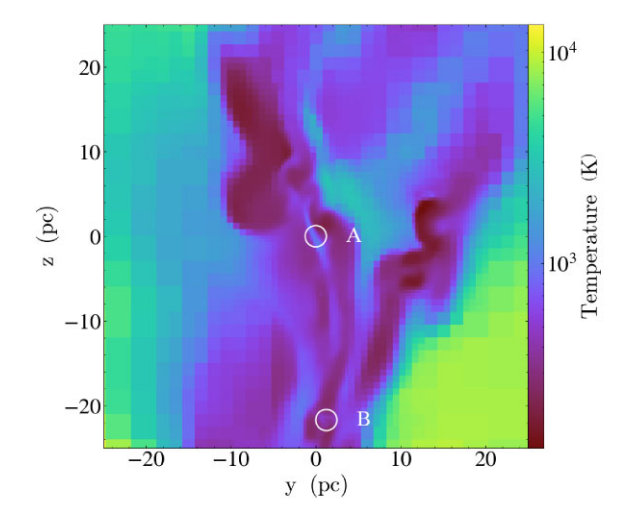
Again, this route requires a strong LW flux to dissociate any H_2 . The critical flux, J_{crit} is set approximately by balancing the dissociation rate of H_2 with the formation rate (Omukai 2001; Shang, Bryan & Haiman 2010; see also the review by Inayoshi et al. 2020). The higher gas densities produced in ACHs increase the H_2 formation

rate. This consequently raises the critical flux required to destroy this H_2 by several orders of magnitude when compared to minihaloes. $J_{\rm crit}$ has been estimated to be in the range of 10^{3-5} J_{21} for ACHs, where $J_{21} = 10^{-21}$ erg s⁻¹ cm⁻² Hz⁻¹ sr⁻¹ (Omukai 2001; Shang et al. 2010; Sugimura, Omukai & Inoue 2014; Wolcott-Green, Haiman & Bryan 2017; Wolcott-Green & Haiman 2019).

This large background radiation could be found in rare, overdense regions with bright, nearby galaxies (Dijkstra et al. 2008). However, it is larger by about two orders of magnitude than the expected background at the time of reionization (Haiman & Loeb 1997; Wise & Abel 2007; O'Shea & Norman 2008). In order to produce this level of LW radiation, we propose supplementing the cosmological background LW radiation, or the high LW flux from neighbouring haloes, with another source. Previous studies have looked at LW radiation from neighbouring (Chon & Latif 2017; Regan et al. 2017) or merging (Visbal, Haiman & Bryan 2014) haloes. Here, we focus on sequential star formation within the cores of individual haloes. We propose that the first star to form within an ACH can produce an additional source of 'internal' LW radiation. If the first protostellar cloud core fails to form a SMS, it can still produce a sufficiently intense LW radiation to irradiate other protostellar cores collapsing nearby, reducing or eliminating H₂-cooling in their vicinity. Here, we examine whether this internal LW feedback could then raise the gas temperatures and help produce the aforementioned environment of warm atomic gas, needed to form a SMS. We emphasize that this is different from the usual LW-driven SMS formation route, in which LW radiation dissociates H2 before the halo's dynamical collapse. Our scenario investigates the possibility of forming SMS stars in haloes that have already begun to collapse and cool due to H₂ cooling. We investigate whether we can indeed dissociate the H₂ at these higher densities and then reheat the gas to the atomic cooling threshold in time to see atomic cooling driven accretion on to our protostar.

We follow up on the high-resolution simulations of Kulkarni, Visbal & Bryan (2019) using the cosmological hydrodynamics code ENZO. They subject three haloes to varying amounts of ionizing flux, studying the impact on the halo's collapse and the stellar history. We study the evolution of one of these haloes, an ACH with a virial mass of $\sim 3.2 \times 10^8 \,\mathrm{M}_\odot$ that produces nearby, sequential star formation. This halo first forms stars well above the atomic-cooling threshold, due to the presence of a strong assumed ionizing radiation background, as described in Section 2 below. The halo has two primary clumps (see Fig. 1 below), which we correspondingly label 'clump A' and 'clump B'. The annotated circles respectively enclose 3000 and 2000 M_☉ within a 1 pc radius around each clump. We perform a new suite of simulations with ENZO, to track the evolution of the highest mass (at the end of the simulation) star within each clump. We investigate how LW radiation from the first star that forms affects the growth of the stars elsewhere in the halo and whether or not a SMS star can form.

To summarize, in this paper, we look at the effects of adding LW radiation from an internal source on the formation of protostellar cores and their subsequent growth. In Section 2, we discuss the set-up of our simulations and how we model and track star formation and evolution. In Section 3, we present analytical estimates for the propagation of LW radiation-driven H₂ dissociation versus the usual atomic H₁ ionization fronts. In Section 4, we first describe the impact of the additional internal LW flux on the formation and growth of protostars in the halo. We then discuss the implications of our findings for SMS and so-called 'direct-collapse BH (DCBH)' formation, including the possibility of forming a SMS under different



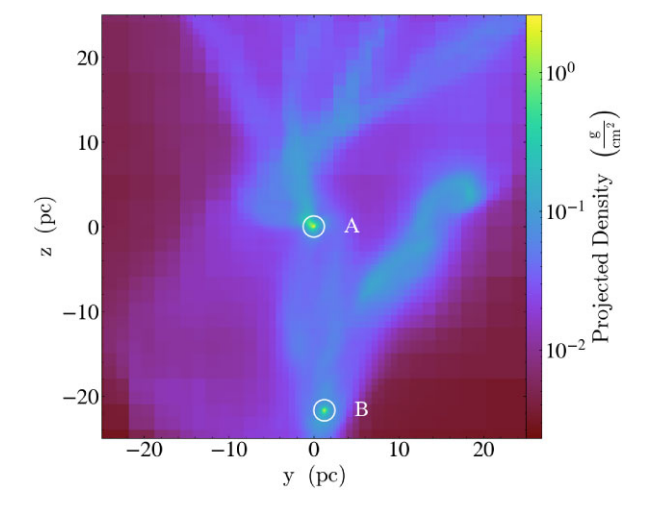


Figure 1. Top: slice of gas temperature along the x-axis and centred on clump A's maximum density gas cell. Bottom: corresponding gas density, projected along the x-axis. Both clumps A and B are circled and labelled. Both the slice and projection are displayed at snapshot #10, z = 6.5648.

circumstances. In Section 5, we summarize our results and our main conclusions.

2 SIMULATION SET-UP

We outline our computational and numerical set-up below. We first briefly describe ENZO, the hydrodynamical code we use. We then detail our test halo's initial conditions and the numerical set-up of our tests. Finally, we specify how we implement LW radiation and measure its effects on sequential star formation within our halo.

We run our simulations using the publicly available adaptive mesh refinement (AMR) code ENZO (Bryan & Norman 1997; O'Shea et al. 2004; Bryan et al. 2014). ENZO tracks dark matter (DM) dynamics using an *N*-body particle mesh solver (Shang et al. 2010) and an Eulerian AMR method produced by Berger & Colella (1989) to solve the ideal gas hydrodynamic equations. We specifically use the spatially third-order accurate Piecewise Parabolic hydro-solver method, which maintains energy conservation. ENZO self-refines when certain criteria are met, dividing cells into eight smaller cells. This allows it to resolve a wide range of dynamic regions more efficiently. Further, it tracks the evolution of nine chemical species

(H, H+, He, He+, He++, H-, H_2 +, H_2 +, and e-) and includes radiative cooling (Abel et al. 1997; Abel, Bryan & Norman 2000). We do not include HD or deuterium molecules since these should not affect the regions we are interested in (McGreer & Bryan 2008; Kulkarni et al. 2019).

We specifically select Halo C produced in Kulkarni et al. (2019) to investigate further. This was one of three haloes produced by individual cosmological zoom-in simulations. Each uses a Lambda cold dark matter cosmology agreeing with Planck Collaboration XVI (2014): h = 0.67, $\Omega_b = 0.049$, $\Omega_m = 0.32$, $\Omega_{\Lambda} = 0.68$, $\sigma_8 =$ 0.83, and $n_s = 0.96$. The simulations were ran in a comoving $2 h^{-1}$ Mpc cosmological box centred around each halo. Halo C was selected from a 256³ grid DM-only simulation. 128³ grid size hydro simulations were then run on each halo. The MUSIC initial conditions generator was set with random seeds that produce matching initial conditions between the 2563 and 1283 grids. The 1283 zoomed hydro simulation had an $836\,M_{\odot}$ DM particle mass. The precise cosmological conditions are specified in Kulkarni et al. (2019). We implement the same hydrogen ionization self-shielding prescription, developed by Rahmati et al. (2013), as Kulkarni et al. (2019) and Visbal, Bryan & Haiman (2017). The H₂ photo-dissociation rate is modified using Wolcott-Green, Haiman & Bryan (2011)'s selfshielding function, as in Kulkarni et al. (2019).

Each halo was subjected to a background ionizing flux of $0.1~F_0$, where $F_0 = 6.7 \times 10^6$ photons s⁻¹ cm⁻². This corresponds to the ionizing flux produced by a $6.6 \times 10^{11} \,\mathrm{M}_{\odot}$ DM halo at $z \sim 7$. This size halo, with the star formation efficiency and escape fraction both 0.1, would produce 2×10^{53} photons s⁻¹ over a redshift range $\Delta z \simeq 10$. This corresponds to the above 0.1 F_0 for a galaxy 50 kpc away (Kulkarni et al. 2019).

The simulation did not use ray-tracing to model the ionizing flux. Instead, it uses an isotropic and uniform radiation field. This is also applied to the 'background' and 'internal' LW fluxes we apply. The background LW radiation is set to 100 J₂₁. This is representative of the background LW field in an overdense region of the universe (Ahn et al. 2009). This background increases in the presence of outside ionizing radiation as $J_{LW} = (100 + 75 \times F/F_0)J_{21}$, with F equaling the ionizing flux (Kulkarni et al. 2019). Our simulation begins at the point Halo C begins runaway collapse, which occurs at z = 6.5648. This collapse time is marked by the simulation reaching refinement level 18. We are therefore modelling a halo whose collapse is delayed due a background ionizing radiation. We note that this atomic cooling halo forms significantly later and is more massive than commonly thought of ACHs. It forms too late for a SMS formed within the halo to grow into a SMBH. However, these facts should not change our general conclusions. We discuss this further in Section 5.

Further, we confirm that there is enough available gas mass to form a SMS if accretion does not fall below the critical accretion rate. We find $10^5\,\mathrm{M}_\odot$ of gas within 21 pc of sink B1. The freefall time, $\sqrt{r^3/GM}$, for this gas is several Myr (Fig. 2). We also plot the ratio of the enclosed mass to the Bonnor–Ebert mass (Fig. 3). The Bonnor–Ebert mass is calculated as $M_\mathrm{BE}\approx 1050\,\mathrm{M}_\odot(T/200\,\mathrm{K})^{3/2}(\mu/1.22)^{-2}(n_\mathrm{H}/10^4\,\mathrm{cm}^{-3})^{-1/2}$, where μ is the mean molecular weight and n_H is the hydrogen number density. We define the cloud mass as the enclosed mass where the above ratio $(M(< r)/M_\mathrm{BE})$ is maximized, following Hirano et al. (2014). This peak does occur near $r=21.8\,\mathrm{pc}$, which corresponds to the distance between sinks A and B1. Even under the conservative assumption that all gas within 4 pc of sink A is gravitationally bound to clump A, this mass ($\sim 1.4 \times 10^4\,\mathrm{M}_\odot$) represents only about 10 per cent of the total mass enclosed around sink B at that distance. We are therefore

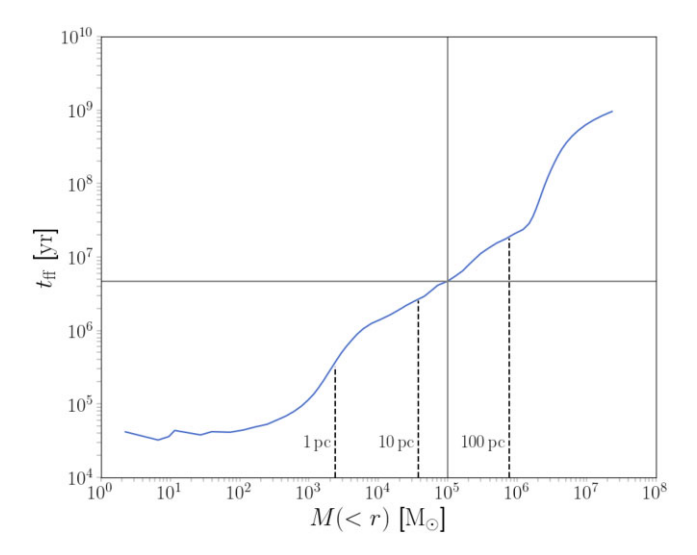


Figure 2. Radial profile of the free-fall time plotted against the enclosed mass, both centred on sink B1. The solid grey lines mark an enclosed mass of $10^5 \, \rm M_{\odot}$ and the corresponding free-fall time, $4.7 \times 10^6 \, \rm yr$. The three vertical dashed lines show the enclosed mass corresponding to radii of 1, 10, and 100 pc. Displayed at snapshot #10, z = 6.5648.

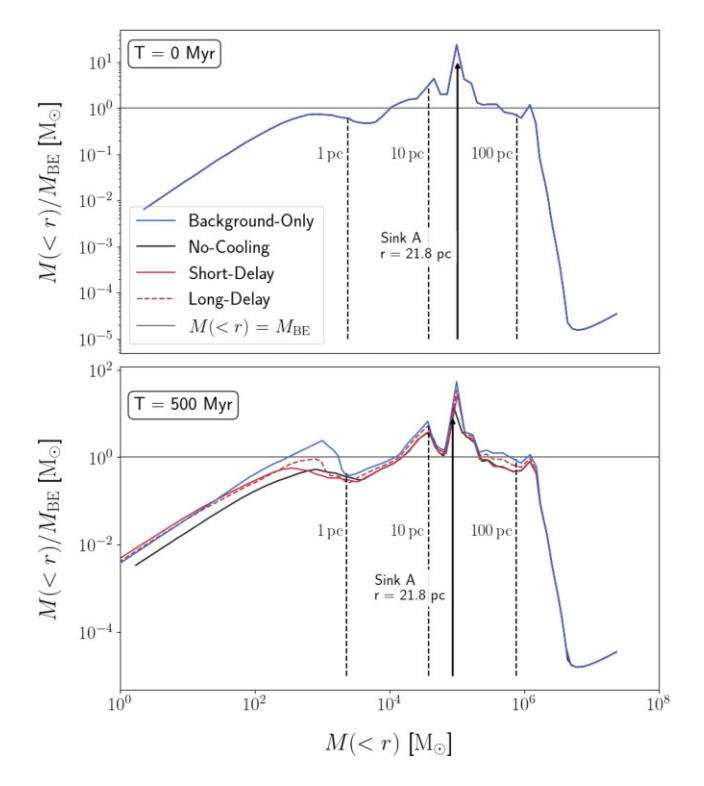


Figure 3. Ratio of the enclosed mass to the Bonnor–Ebert mass plotted against the enclosed mass. Both the enclosed mass and Bonnor–Ebert mass profiles are centred on sink B1 for the background-only, short-delay, and long-delay runs. We centre the profiles on clump B's density maximum in the no-cooling run, which does not form sink B1. The top panel shows this profile at t=0 yr, while the bottom profile panel displays it at $t=5\times10^5$ yr. The grey horizontal line marks a ratio of 1. The ratio peaks at $M(< r) > 10^5 \, {\rm M}_{\odot}$, showing there is a sufficiently massive unstable self-gravitating gas cloud to potentially form a SMS. The solid black arrow indicates the enclosed mass and $M(< r)/M_{\rm BE}$ ratio at r=21.8, the distance to sink A. Vertical dashed lines again indicate the enclosed mass corresponding to radii of 1, 10, and 100 pc.

Table 1. Parameters of the four test runs described in Section 2. We list the run names, the intensity of the additional 'internal' LW flux, and the delay with which we add them after the simulation (re)start.

Run	'Internal' $J_{ m LW}$	t _{delay} (yr)
Background-only	0	n/a
Short-delay	10^{4}	20 000
Long-delay	10^{4}	250 000
No-cooling	10^{10}	0

confident that there is a massive cloud of unstable self-gravitating gas on order $10^5\,M_\odot$, which is necessary to fuel SMS formation. This also holds true for the gas cloud surrounding sink A. The key limitation for SMS formation thus becomes the protostar's accretion rate, rather than the quantity of gas available nearby.

We use ENZO's 'sink' particle mechanism to model star formation and evolution. Sink particles have been previously used to simulate the first generation of stars in grid-based and smoothed-particle hydrodynamics codes (Krumholz, McKee & Klein 2004; Stacy, Greif & Bromm 2010; Greif et al. 2012; Stacy 2012). We add a sink particle to a cell when it reaches the highest refinement level and wants to evolve further. The accretion rate is set so that the maximum density of a cell in a spherical region with radius < 5 cell widths cannot exceed the maximum level of refinement. This avoids artificial fragmentation due to forming sinks very close together. We set the maximum refinement level to 18, matching the runs of Kulkarni et al. (2019). Additionally, sink particles merge if the distance between them decreases below 10 times the width of the smallest cell. This sink particle method, used in Kulkarni et al. (2019), produced similar results to more sophisticated sink particle algorithms, i.e. Regan & Downes (2018). We are therefore confident in adopting it to this work. We track the sink particle 'properties' using our data snapshots, which have $\sim 10^4$ yr temporal resolution.

We include four separate runs in our work (Table 1). Again, each begins at runaway collapse in Halo C from Kulkarni et al. (2019). The first run ('background-only') proceeds from this point for roughly 1 Myr. We do not include any additional LW flux, setting this up as the benchmark to compare sink particle formation and evolution with and without additional LW radiation. The second run ('short-delay') implements LW radiation immediately at the simulation (re)start. It ramps up linearly from no additional LW radiation at the simulation restart to 10⁴ J₂₁ in 20 000 yrs. This represents a star 'turning on' very quickly after the runaway collapse begins within the halo. It then irradiates the halo with photons in the LW band. The third run ('long-delay') delays adding the additional LW flux by 250 000 yrs. The flux then increases from the background level to $10^4 \, \mathrm{J}_{21}$ at this time. This represents a case in which a protostar forms somewhat later and then eventually settles on to the main sequence before producing LW radiation. The 10⁴ J₂₁ flux is chosen as the flux since it corresponds to the LW flux produced by a \sim 150 M_{\odot} Pop III star over its lifetime (several Myr) at a distance of 20 pc away, approximately the distance between our two clumps of gas.

We find that none of these three initial runs fully dissociate the $\rm H_2$ in the high density regions surrounding the sink particles. We therefore introduce a much higher (artificial) LW flux of $\rm 10^{10}\,J_{21}$ in our fourth run to fully dissociate $\rm H_2$ in the highest density regions and investigate the effect on star formation. This run ('no-cooling') effectively removes molecular cooling in the halo, and allows us to address whether the gas in the halo is able to dynamically heat to the atomic cooling threshold and activate HI cooling to form a supermassive star.

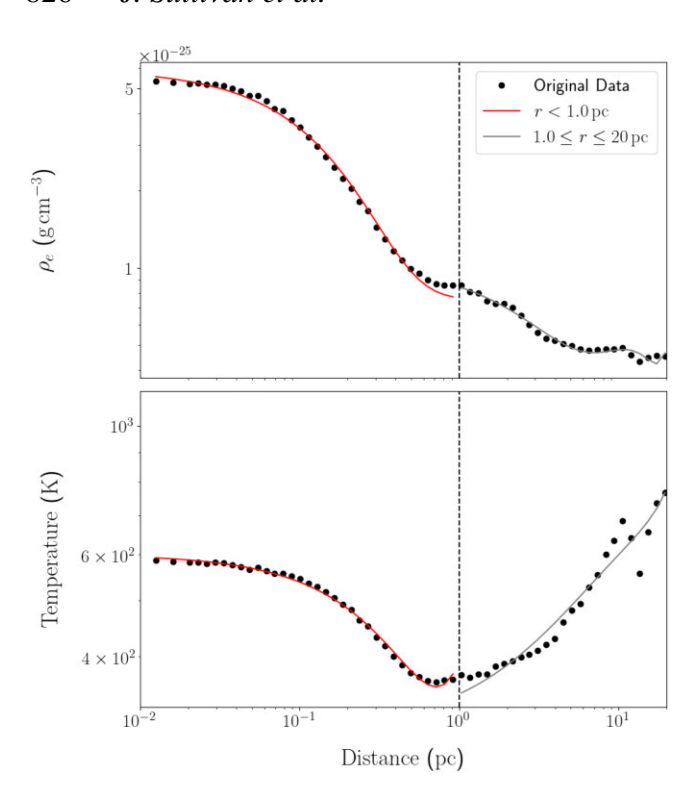


Figure 4. Analytical fits to radial electron density (top) and gas temperature (bottom) profiles centred on clump A. The fit for r < 1.0 pc is plotted in red and the fit for $1.0 \le r \le 20 \,\mathrm{pc}$ is plotted in grey.

3 ESTIMATING THE PROTOSTAR'S SPHERE OF INFLUENCE

We first analytically treat the problems of H₂ dissociation and H ionization within the halo. We estimate the time it would take for a dissociation and ionization front to travel from the centre of clump A, host of the first protostar, to the centre of clump B, where the second protostar is forming \sim 20 pc away. We follow the standard H-ionization front (e.g. equation 5 of Kulkarni et al. 2019):

$$4\pi R^2 n(R) dR = \left(\dot{N}_{\text{ion}} - 4\pi \alpha \int n^2(r) r^2 dr \right) dt, \tag{1}$$

where R is the radius of spherical shells, n(R) is the hydrogen number density, $\dot{N}_{\rm ion}$ is the ionizing photon rate, and α is the case-B recombination rate coefficient at 10^4 K. r is defined as the distance away from the clump centre or the sink particle, once it has formed. The number density of hydrogen is measured in the simulations in two regions, 0–0.1 and 0.1–20 pc. This covers the distance between clumps A and B in Halo C (Fig. 1). To calculate the dissociation of molecular hydrogen, we employ the analogous equation:

$$4\pi R^2 n_{\rm H_2}(R) dR = \left(0.1 \,\dot{N}_{\rm LW} - 4\pi \,k_9 \int n_{\rm H} n_{\rm e}(r) r^2 dr\right) dt,\tag{2}$$

where k_9 represents the rate for H⁻ formation through the combination of H and e⁻, $k_9 = 6.775 \times 10^{-15} \text{ T}_{\text{eV}}^{0.8779}$, which is the bottleneck reaction in gas-phase H_2 -formation (Shang et al. 2010). n_H , n_{H_2} , and n_e represent the atomic hydrogen, molecular hydrogen, and electron number densities, respectively. We multiply the number of LW photon's produced per second, \dot{N}_{LW} , by 0.1 because roughly 10 per cent of collisions between LW photons and H2 dissociates the

We use the hydrogen number density from Kulkarni et al. (2019): $n_0(r/r_{\rm pc})^{-2}$, with $r_c = 0.1 \,\mathrm{pc}$, for $r > 0.1 \,\mathrm{pc}$ and n_0 for $r < 0.1 \,\mathrm{pc}$

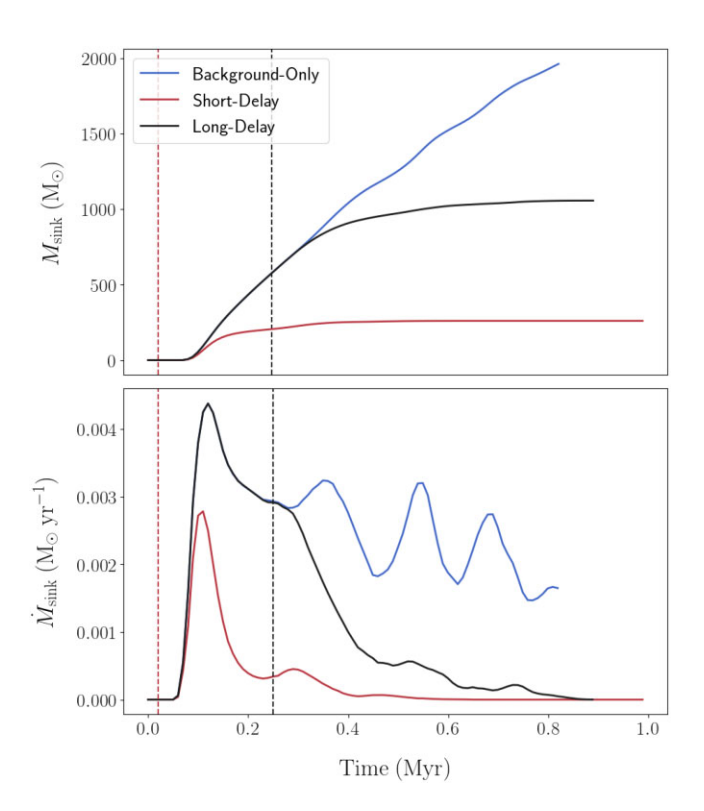


Figure 5. The top panel displays the sink B1's mass and the bottom panel displays its accretion rate as a function of time for each run. t = 0 is defined as the (re)start of the simulation at z = 6.5648. The three solid coloured lines represent the three test runs. The vertical dashed lines represent when the additional internal LW flux is added in the short- (left) and long-delay (right) runs, respectively. When internal LW radiation is introduced, the accretion rate rapidly decreases and the masses reach significantly lower values than in the background-only run.

0.1 pc, where $n_0 = 1.04 \times 10^{-6} \, \text{cm}^{-3}$. The electron number density is produced by creating a spherically averaged profile centred on clump A. The electron density is then fit logarithmically in the region 0-1 pc, and a 3rd-order polynomial in the region 1-20 pc (Fig. 4). This yields the two expressions:

$$o_{e}(r) = \begin{cases} 5.19 \times 10^{-25} \text{ exp}(-6.42r_{\text{pc}}) & \text{if } r_{\text{pc}} < 1.0 \\ +7.57 \times 10^{-26} \text{ g cm}^{-3} & \\ 4.542 \times 10^{-30} r_{\text{pc}}^{4} - 2.131 \times 10^{-28} r_{\text{pc}}^{3} & \\ +3.503 \times 10^{-27} r_{\text{pc}}^{2} - 2.397 \times 10^{-26} r_{\text{pc}} & \text{if } 1.0 \le r_{\text{pc}} \le 20 \\ +1.051 \times 10^{-25} \text{ g cm}^{-3}, \end{cases}$$

$$(3)$$

where $r_{\rm pc}$ is the distance in parsecs. We model the temperature in both regions with 3rd-order polynomials (Fig. 4), producing the two analytical approximations:

$$T(r) = \begin{cases} 26.387 \, r_{\rm pc}^3 + 437.44 \, r_{\rm pc}^2 & \text{if } r_{\rm pc} < 1.0 \\ -670.57 \, r_{\rm pc} + 600.39 \, \text{K} \\ 6.3571 \times 10^{-2} \, r_{\rm pc}^3 - 2.52522 \, r_{\rm pc}^2 \\ +49.0274 \, r_{\rm pc} + 298.068 \, \text{K} & \text{if } 1.0 \le r_{\rm pc} \le 20. \end{cases} \tag{4}$$

These values are used for k_9 , which is a function of temperature (Shang et al. 2010). The flux of LW photons is calculated assuming 6.5×10^4 LW photons per baryon for a Pop III star (Feathers et al. 2024). For a 150 M_☉ star with a lifetime of 2 Myr, this becomes 1.84×10^{50} LW photons per second. This corresponds to $10^4 \, \mathrm{J}_{21}$ at a distance of 20 pc, the distance between the two gas clumps in our simulation.

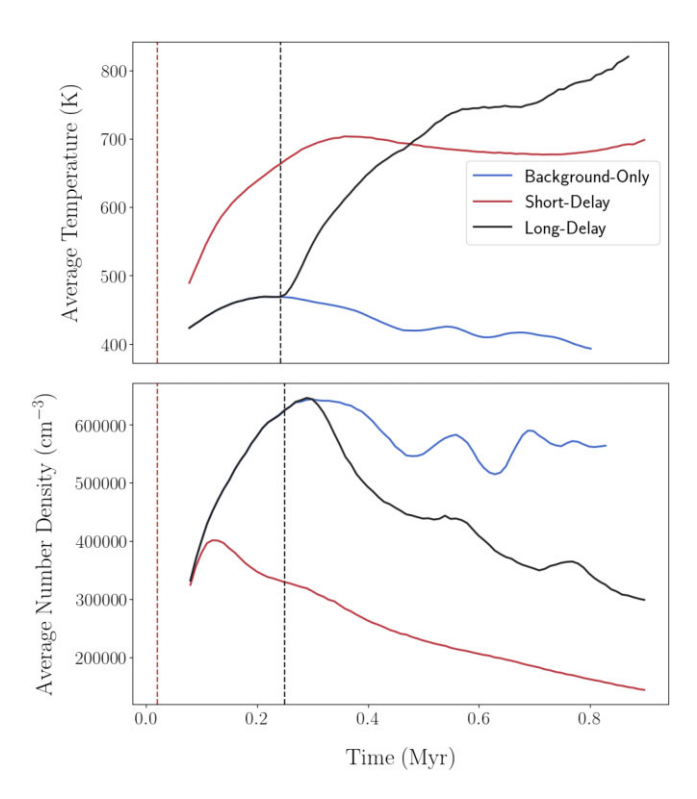


Figure 6. The top and bottom panels show the evolution of the average temperature and density within 1 pc of sink B1, respectively. The lines represent the background-only, short-delay, and long-delay runs, as in Fig. 5. The temperature again rises significantly immediately after additional LW is introduced. However, the short-delay temperature peaks at and then settles near $T=700\,\mathrm{K}$. The temperature continues to climb in the long-delay run throughout the simulation time, reaching $T=820\,\mathrm{K}$. The densities decrease with the additional LW flux.

Ultimately, the number of dissociating photons outweighs the production of new H_2 and we find that the time it takes for the full sphere to be dissociated is $\sim 1.5 \times 10^2$ yr. This analytical result does not fully take into account self-shielding or the progression of this front at different speeds (based on density or other local properties). However, it shows promise for the ability of LW photons to promptly dissociate H_2 in the regions around forming stars/sink particles.

We then checked the time it would take for an ionizing front to sweep over this same spherical shell. This is useful to determine the treatment of ionizing feedback when creating star particles. We again use equation (1), now assuming $n_{\rm p}=n_{\rm H}=n_{\rm e}$ in the ionized region. The temperature is set to the atomic cooling limit, $\sim 10^4$ K. Ionizing photons have energies >13.6 eV, but their number flux is comparable to the LW flux. $\dot{N}_{\rm ion}$ is therefore set to the previous $\dot{N}_{\rm LW}$ value.

We find that the recombination rate outweighs the ionization rate and that this ionization front cannot propagate to the second clump. Kulkarni et al. (2019) uses a more detailed analytical set-up to estimate the propagation of the ionization front, and find it takes ~ 2 Myr to travel 20 pc. Since this is beyond the simulated time period in our simulation, we feel comfortable not including UV radiation/feedback. Correspondingly, we do not artificially heat the halo to simulate this ionization heating.

4 RESULTS AND DISCUSSION

In this section, we first describe in detail the results of Table 1's first three runs (Sections 4.2-4.4). We explain the fourth run's addition and its results in Section 4.5. We first briefly discuss fragmentation and its relevance to the subsequent results. We then analyse clump B, which forms a sink particle after clump A. This follows the goal of this work, examining how the introduction of an additional LW flux impacts sequential star formation. Clump B is the second highdensity clump, located at the bottom of Fig. 1. We initially look at the masses and accretion rates of the largest sink particle, 'sink B1', within this clump. We also look at the gas properties that influence the sink particles' growth. This includes the gas temperature, gas number density (encompassing the nine chemical species listed in Section 2), H_2 fraction $(X_{\rm H_2})$, and electron fraction $(X_{\rm e})$. Lastly, we briefly summarize the effect of the LW radiation on clump A. This is the high density clump at the centre of Fig. 1 and it contains the first protostar that forms, sink A1. We can analyse the additional LW flux's impact on clump A in the same way as clump B due to us implementing a uniform background flux. Studying clump A demonstrates what would happen if it was the 'secondary' clump subject to an additional LW flux from a hypothetical neighbouring protostar. Even though there is no such previously-formed star in our simulation, the differences in gas density and temperature between clumps A and B provide a useful additional data point to study the LW radiation's effect on gas and star formation in different environments.

4.1 Fragmentation

We observe fragmentation, defined by the number of sink particles that form, across our three initial runs. This fragmentation is largest in the background-only run, followed by the long-delay and finally the short-delay run. In the short-delay run, adding the LW flux to clump B before sink B1 forms eliminates any additional sink particle formation. This supports the expectation that the LW radiation reduces fragmentation and matches the result below that the internal LW flux inhibits cooling across the two clumps. The fragmentation does not affect our main results in any of these runs. The first sink particles to form in each clump, sink A1 and B1, remain the most massive sink particles across the simulated time. We therefore restrict our focus to these two sink particles.

4.2 Clump B

We investigate how adding an additional LW flux affects clump B and the protostar that forms within it. We first look at the protostar's growth and then its local gas properties such as temperature, density and $X_{\rm H_2}$. We track these values beginning at our snapshot #17, 7 × 10^4 yr after the (re)start of our simulation (snapshot #10). This is the first snapshot to contain a sink particle in clump B. It is also $t = 6 \times 10^4$ yr years after the first sink particle (sink A1) forms in clump A. The total number of snapshots varies between runs, the shortest being 74 ('background only') and the longest being 110 ('no cooling').

4.2.1 Accretion rate and protostellar mass

We calculate and plot sink B1's mass and accretion rate versus time (Fig. 5) to measure how the additional LW flux affects the sink particle's growth. We do not observe the expected increase in accretion rate and sink particle mass when the additional flux is added – we instead find the opposite trend.

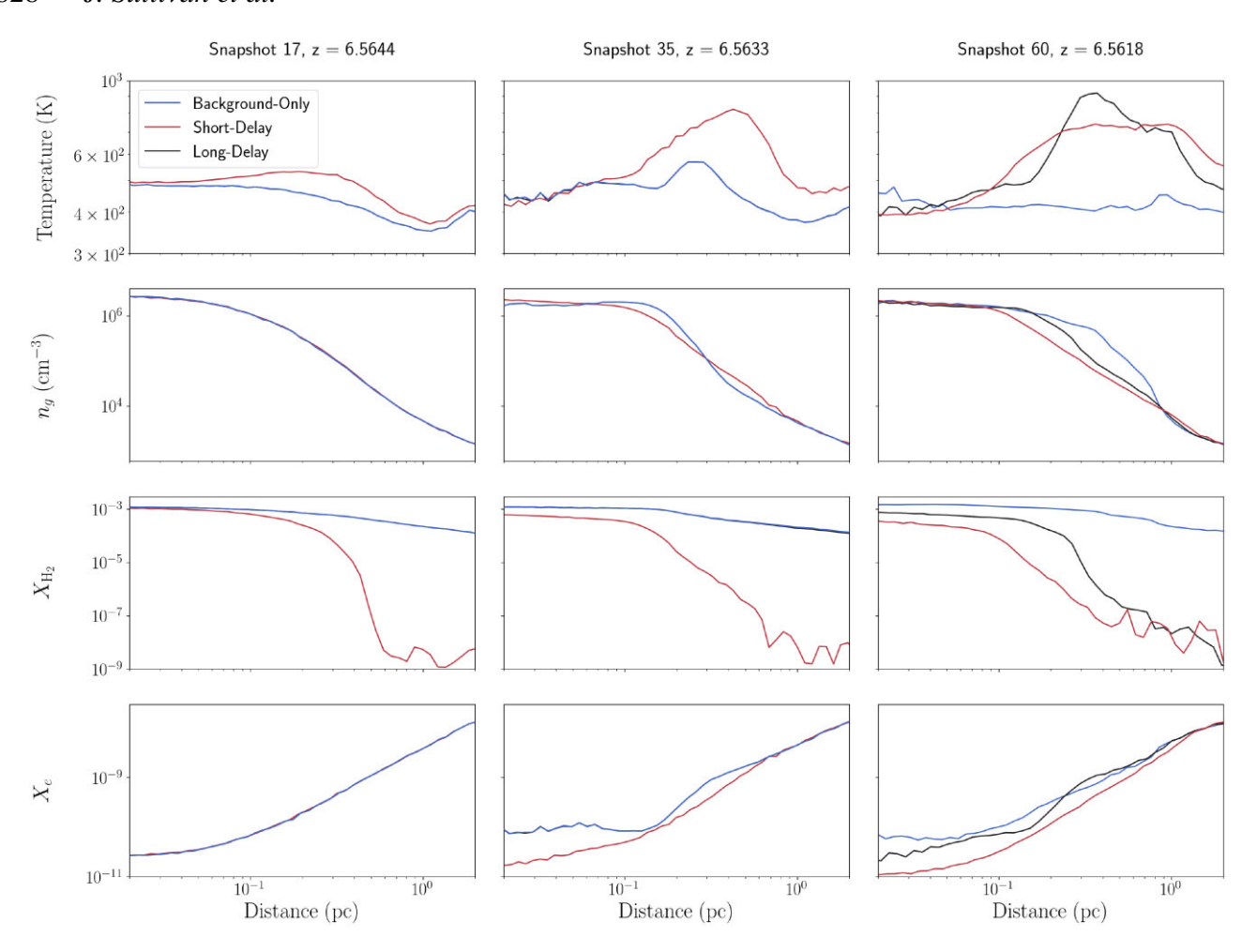


Figure 7. From top to bottom: radial profiles of temperature, gas number density, $X_{\rm H_2}$, and $X_{\rm e}$ centred about sink B1. From left to right, the columns display the profiles at snapshot #17 (z = 6.5644, $\sim 6 \times 10^4$ yr after sink A1 forms in snapshot #11), 1.8×10^5 yr later at snapshot #35 (z = 6.5633), and an additional 2.5×10^5 yr later at snapshot #60 (z = 6.5618). The lines represent the background-only, short-delay, and long-delay cases, respectively. Snapshot #35 (middle column) displays the effects of the additional LW flux in the short-delay run just before the time when the additional LW flux is added in the long-delay run. We see the influence of the additional LW flux in both the short-delay and long-delay runs in snapshot #60 (right column). We see increases in temperature in the short and long-delay runs. However, the clump's innermost region retains a low temperature. The background-only run maintains the highest temperature at the clump centre. We see different shifts in gas number density after the internal LW flux is added. The density is slightly raised above the background-only run at the centre and outermost regions but decreases more significantly over the majority of the clump's volume. $X_{\rm H_2}$ also decreases after the additional flux is added. However, this decrease is highly sensitive to the gas density. It remains high close to sink B1, where the gas density is highest, and drops off rapidly at the lower densities further from the clump centre. The short-delay run has a reduced electron fraction relative to the background-only run until roughly 1 pc. In the long-delay run, $X_{\rm e}$, is only reduced relative to background-only run at low r.

In the background-only run, sink B1's mass climbs to roughly $2000\,M_\odot$ within $8.4\times10^5\,\mathrm{yr}$ and is continuing to grow at the time we end the simulation (Fig. 5). However, the accretion rate peaks at $4.4\times10^{-3}\,M_\odot\,\mathrm{yr}^{-1}$ and then fluctuates between $\sim\!(2-3)\times10^{-3}\,M_\odot\,\mathrm{yr}^{-1}$. This remains well under the minimum rate to delay collapse on to the main sequence, $0.01\text{--}0.04\,M_\odot\,\mathrm{yr}^{-1}$. We therefore expect to see this protostar settle on to the main sequence at lower masses or fragment into several low mass stars.

In the two other runs, the sink particle mass quickly flattens out after the additional LW flux is introduced. In the short-delay run, the LW flux decreases the observed accretion peak measured in the background-only run. The accretion rate then continues to decrease and effectively stops by 6.7×10^5 yr (Fig. 5). The mass in the short-delay run therefore plateaus at $260\,\mathrm{M}_\odot$, significantly lower than in the background-only run. We see that the additional LW flux produces a smaller protostar, rather than the desired more massive one.

In the long-delay run, this trend is the same. However, the accretion rates and masses diverge after the initial peak in accretion rate due to the delay in the additional LW flux being introduced. Once the additional flux is added, the accretion rate quickly falls to $\lesssim\!10^{-3}\,M_\odot\,yr^{-1}$ by $4\times10^5\,yr.$ The rate continues to decrease until accretion stops, as in the short-delay run. The final mass value flattens out at $\sim\!1000\,M_\odot$. We see that delaying the additional flux does not increase the likelihood of a massive star forming. The increase in final mass compared to the short-delay run is simply due to delaying the decrease in the accretion rate.

4.2.2 Density and temperature near the protostar

We measure the average gas temperature and density in a 1 pc region centred on sink B1, to display how the LW flux affects a wider region. The average temperature of this region increases significantly

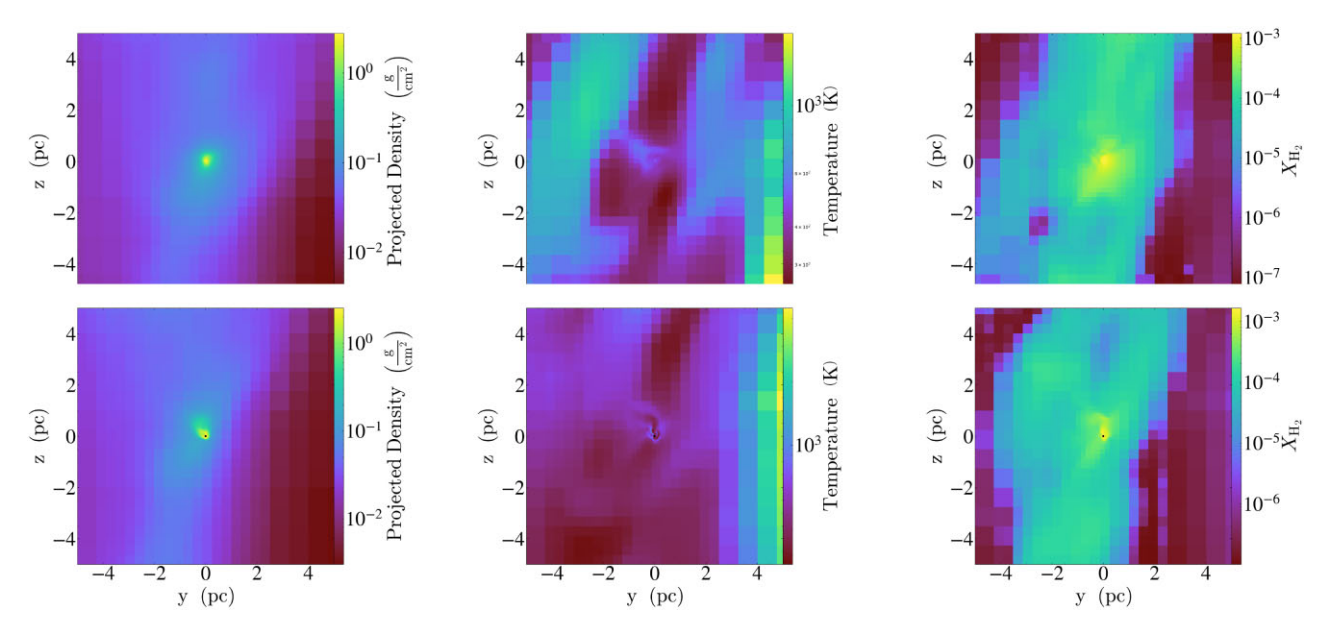


Figure 8. From left to right: projection of density, slice of temperature, and slice of the $X_{\rm H_2}$ along clump B's x-axis in the background-only LW run. The top row displays these plots at snapshot #17, 7×10^4 yr after the simulation start, centred about sink B1. The bottom row displays these values at snapshot #60, 4.3×10^5 yr later.

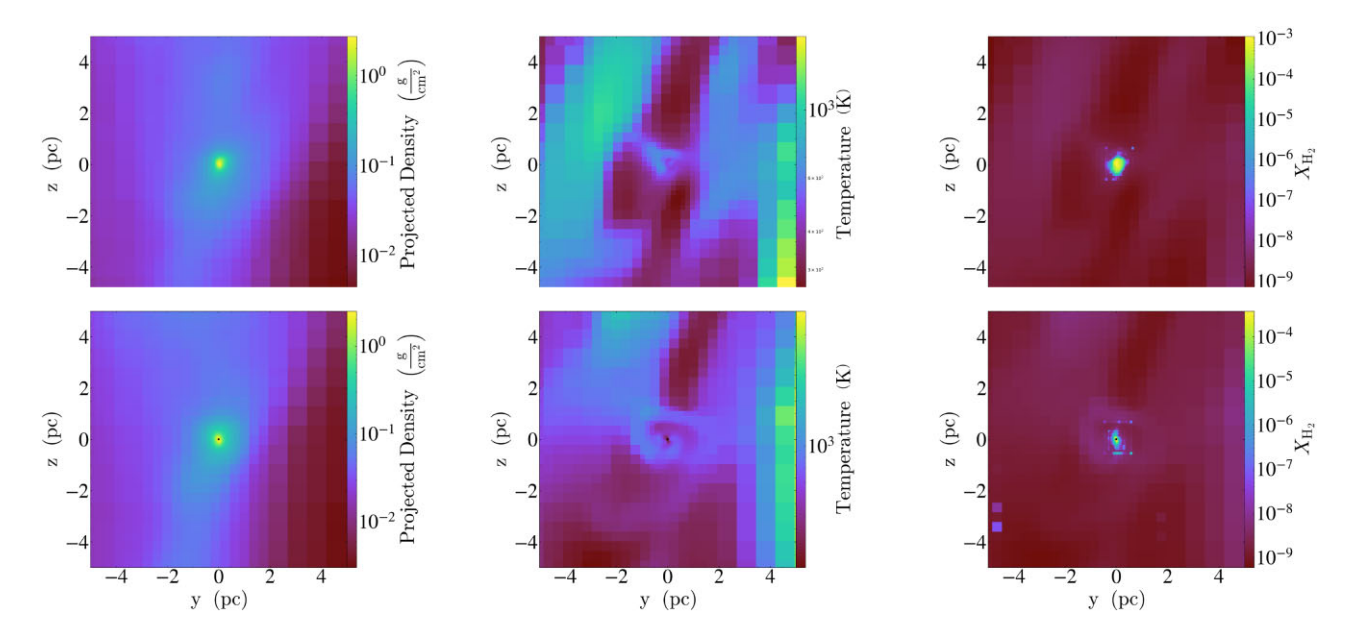


Figure 9. Same as Fig. 8 except displaying the short-delay run.

above the background-only run when the additional LW flux is added (Fig. 6). The average temperature in the background-only run heats up to 469 K and then slowly decreases past 400 K by $t=8.4\times10^5$ yr. The short-delay produces an average temperature that settles at $T\simeq700$ K. The average temperature in the long-delay is at 820 K and continuing to rise at the time the run ends ($t=9\times10^5$ yr). We therefore see that the additional LW flux does diminish cooling within the clump. The average densities clearly decrease with the additional LW flux (Fig. 6). Furthermore, this decrease in density relative to the background-only run continues throughout the simulation. This results in densities a factor of $\sim2-3$ lower in the short- and long-delay runs.

4.2.3 Effects on clump B's gas morphology

Finally, we provide 1D profiles that display some of the changes in temperature, density, $X_{\rm H_2}$, and $X_{\rm e}$ over a 2 pc region (Fig. 7). These profiles are centred on sink B1 and are spherically averaged. We choose a 2 pc radius because this covers a large region of the wider clumps A and B. This is evidenced by the large range of gas number densities covered by the resulting spherical profiles (see Fig. 7 for clump B and Fig. 13 for clump A). We show the initial profiles at snapshot #17, z = 6.5644. We then display the point we turn on the additional LW in the long-delay case, 2.5×10^5 yr after the simulation (re)start. By this point, we see a difference in the short-delay run due to the additional LW. Finally, we show the distributions

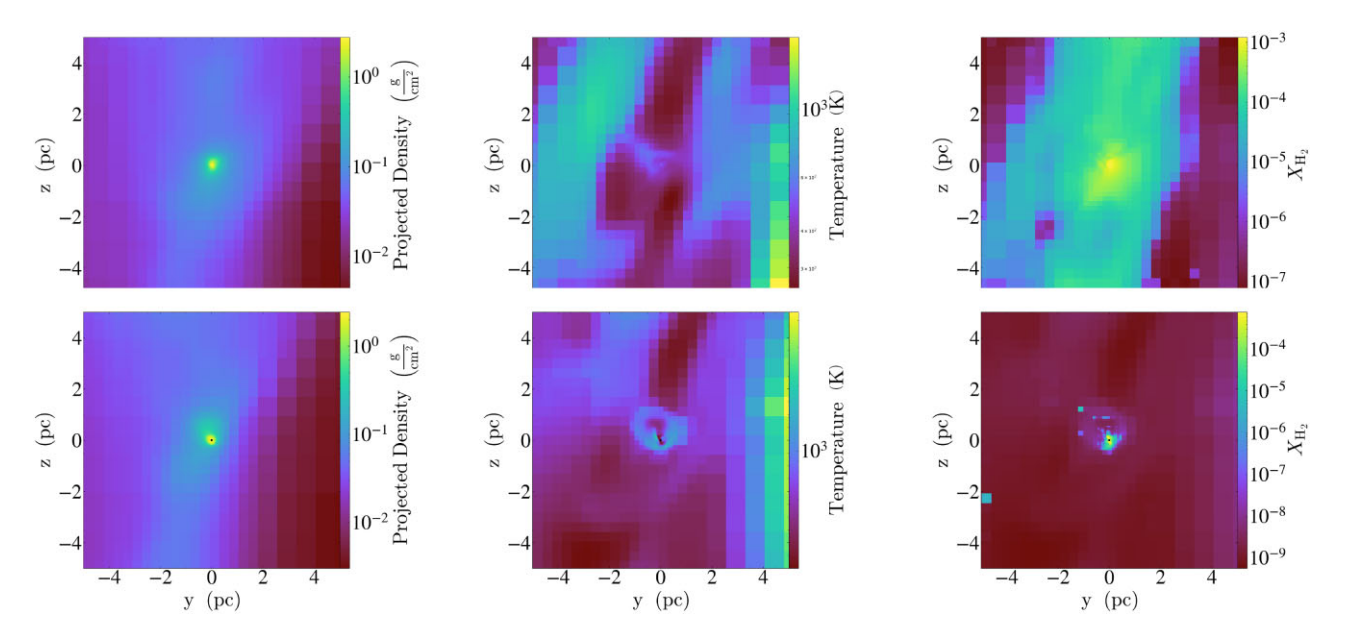


Figure 10. Same as Figs 8 and 9 except displaying the long-delay run.

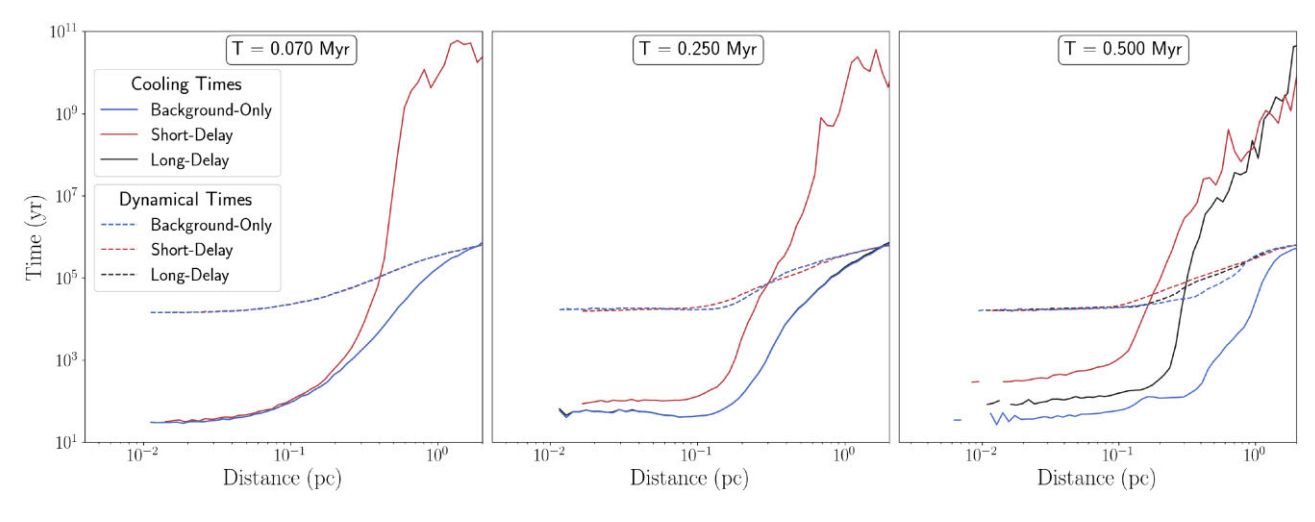


Figure 11. From left to right, the three panels show radial profiles of the cooling time (t_{H_2}) and dynamical time (t_{dyn}) at snapshot #17 (z = 6.5644), 1.8×10^5 yr later at snapshot #35 (z = 6.5633), and an additional 2.5×10^5 yr later at snapshot #60 (z = 6.5618). The solid lines represent the cooling times, while the dotted lines represent dynamical times. Both are plotted for the background-only, short-delay, and long-delay runs. The LW flux clearly increases the cooling time of the gas surrounding sink B1. This produces cooling times longer than the dynamical time slightly outside of the sink particles position. This point of intersection gets pushed further in with time as the gas continues to heat.

an additional $2.5\times10^5\,\mathrm{yr}$ later, by which point both the short- and long-delay runs display differences.

The radial profiles for temperature and density display that gas at different radii is affected differently by the LW radiation (Fig. 7). Close to the sink particle, the additional LW flux in the short-delay run raises the gas temperature slightly higher than in the background-only run (row 1, Fig. 7). We see by the second column, at snapshot #35, the central temperature is lower for the short-delay run. However, this flips as the distance from the sink particle increases. The LW flux raises the gas temperature of the majority of the spherical region above that of the background-only run. This is again seen in snapshot #60 for both of the additional LW flux runs. The LW flux is only able to raise the gas temperature outside of the clump's centre. The observed temperature decrease at small radii produced by the additional LW radiation implies that the additional

flux hurts the sink particle's ability to become a supermassive star.

The density profile also shows that the LW flux impacts the clump differently further away from the sink particle (row 2, Fig. 7). Looking at snapshot #35, the additional LW flux raises the density above the background-only run's at the centre and in a small region further away. However, there is a region in between where the density is decreased by the additional LW flux. We see that the decrease in density here is large enough to produce the decrease in our clump's average density (Fig. 6). This becomes more clear in snapshot #60, which shows a large decrease in gas density further away from the sink particle when the additional LW flux is present.

We next show $X_{\rm H_2}$ to check whether the LW flux successfully dissociates ${\rm H_2}$ (row 3, Fig. 7). The fraction changes drastically as the distance from the sink particle increases. At snapshot #35 in the short-

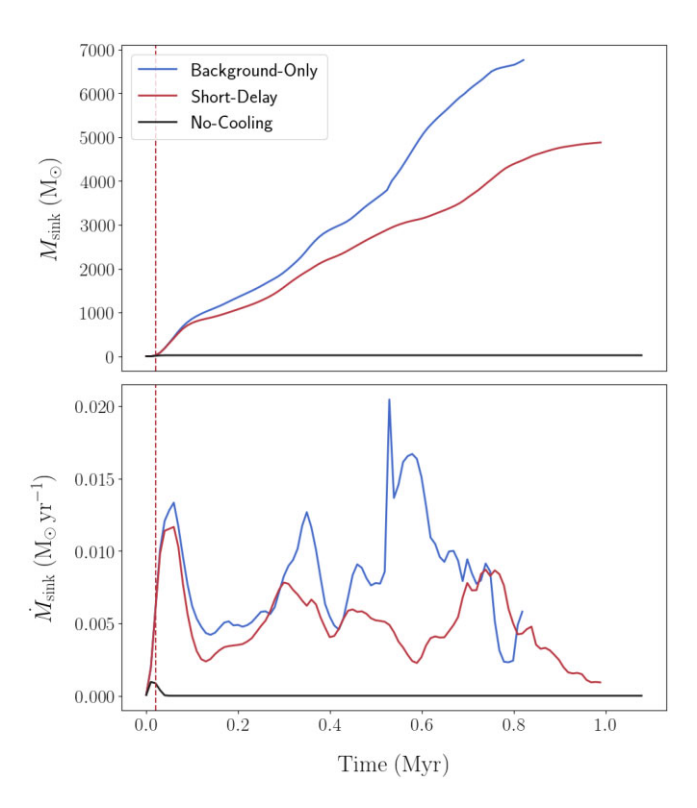


Figure 12. The evolution of sink A1's accretion rate (bottom panel) and its mass (top panel) in the background-only, short-delay, and no-cooling runs. The time is again defined as in Figs 5–6. The additional internal LW flux decreases the sink's accretion rate and final mass in the short-delay run. In the no-cooling run, the accretion shuts off soon after the flux is added and the mass stalls at $23\,\mathrm{M}_\odot$.

delay run, $X_{\rm H_2}$ decreases from $\sim 1 \times 10^{-3}$ to $\sim 2 \times 10^{-4}$ by 0.25 pc and is roughly 5 orders of magnitude lower by 0.5 pc. By comparison, the fraction in the background-only case is $\sim 4 \times 10^{-4}$ at 0.5 pc and greater than \sim 6 \times 10⁻⁴ at 0.25 pc. However, the central $X_{\rm H_2}$ remains high for the short-delay run. This is also apparent in the long-delay run at snapshot #60. $X_{\rm H_2}$ drops off sharply past \sim 0.2 pc, eventually reaching fractions on the order of 10^{-8} . $X_{\rm H_2}$ in the backgroundonly case remains above 10^{-4} out to the edge of our 2 pc sphere. We clearly see that at large distances, the LW flux is effective in dissociating H_2 down to low fractions $\lesssim 10^{-8}$ (Fig. 7). However, the additional LW flux does not efficiently dissociate H2 close to the sink particle. The central fraction in snapshot #35 is only a factor of ~two lower in the short-delay run. At snapshot #50, the central $X_{\rm H_2}$ in the short-delay run has further decreased to $\sim 5 \times 10^{-4}$. The central fraction is $\sim 1 \times 10^{-3}$ for the long-delay case, as compared to $\sim 1.4 \times 10^{-3}$. The gas still cools through molecular cooling at these high $X_{\rm H_2}$ values. We have thus simply slowed the cooling process rather than halting it at the sink particle's location. Finally, the electron fraction, X_e , decreases near the sink particle after the LW flux is added (Row 4, Fig. 7). In snapshot #35, this decrease in the short-delay case extends to \sim 0.8 pc. By snapshot #50, the decrease is visible in both the additional LW runs. Xe is lowered relative to the background-only run past ~1 pc for the short-delay run and out until \sim 0.2 pc for the long-delay run.

We further illustrate the internal LW flux's affect across clump B in Figs 8-10. The figures display a projection of density, slice of temperature, and slice of $X_{\rm H_2}$ centred on sink B1. It displays these for snapshots #17 (top row) and #60 (bottom row) in the initial three runs.

4.3 Cooling and dynamical collapse in clump B

Contrary to our expectations, the LW radiation ultimately has a negative impact on the sink particle mass and accretion. This is tied to the inability to dissociate the $\rm H_2$ in the clump centres, as described above. The gas will continue to cool via $\rm H_2$ in these high density regions. We are thus left with a core of dense and cold gas accreting on to the protostar. Outside of this core, we do dissociate $\rm H_2$ and the gas temperature rises above several hundred K. However, it does not surpass 1000 K, which is well below the atomic cooling threshold. This suggests that the dynamical time within the clump may be too large for us to see elevated infall and accretion rates within our simulation time, even if we fully dissociate $\rm H_2$ around the sink particles.

We first explore the inability to dissociate H_2 in the dense region around the sink particle. We can estimate the ' H_2 survival density', the gas density at which the H_2 will not be dissociated, by balancing the H_2 dissociation and formation rates from equation (2). We use rate k_{28} from Shang et al. (2010) for the H_2 dissociation rate. This creates the following relationship between the dissociation rate and the recombination rate per H_2 molecule: $10^{-12}\beta$ $J_{21}=k_9\frac{n_{H_2}n_e}{n_{H_2}}$, where $\beta=0.9$. We then select values for temperature (used in k_9), n_e , and n_{H_2} . For this estimate, we use values from snapshot #35 in the short-delay run. We select values at a radius of ~ 0.25 pc, where we observe the X_{H_2} begin to drop off (Fig. 7). We define the X_{H_2} cut-off as 10^{-5} . Using $n_e \cong 0.2$ cm⁻³ and $T \cong 800$ K produces a hydrogen number density $n_H \cong 1.4 \times 10^5$ cm⁻³. The densities at the centre of our clumps are significantly higher. We would thus need a much higher LW flux to dissociate the H_2 in these high density, central regions.

We next calculate the cooling and dynamical times. We compute the cooling time as

$$t_{\rm H_2} = \frac{1.5 \, n_{\rm g} \, k_{\rm B} \, T}{\Lambda \, n_{\rm H} \, n_{\rm H_2}},\tag{5}$$

where $n_{\rm g}$ represents the total gas number density. The cooling rate is defined using Galli & Palla (1998)'s analytical expression for gas in the low density limit:

$$\log \Lambda_{\rm H_2} = -103.0 + 97.59 \log T - 48.05 (\log T)^2 + 10.80 (\log T)^3 - 0.9032 (\log T)^4,$$
 (6)

where *T* is the gas temperature in Kelvin and $10 \text{ K} \le T \le 10^4 \text{ K}$. The dynamical time can be estimated as $t_{\text{dyn}} = \frac{1}{\sqrt{4\pi G \rho}}$, where *G* is the gravitational constant, and ρ is the gas density.

The internal LW flux raises the cooling time above the dynamical time in the gas surrounding the sink particle (Fig. 11). This confirms our earlier analysis that the internal LW flux inhibits the gas's ability to cool and accrete on to the protostar. Our protostar should join the main sequence before it reaches masses on the order of $10^3\,M_\odot$ or above. This is motivated by it accreting below the critical accretion rate substantially longer than the Kelvin–Helmholtz contraction time which is on order $\sim\!10^{4-5}\,\mathrm{yr}$ (see fig. 1 of Hirano & Bromm 2017) for a $10{-}100\,M_\odot$ protostar. We thus do not continue the simulations long enough to see the infall of mass on the order of $10^5\,M_\odot$, which takes several Myr to occur.

The cooling time surpasses the dynamical time further away from the sink particle, where the gas density and $X_{\rm H_2}$ decrease. This implies that in these lower density regions, there may be time for the gas to heat to higher temperatures by compression as it begins to collapse, but one must then consider the UV radiation from the central star. However, this prompts a different scientific question

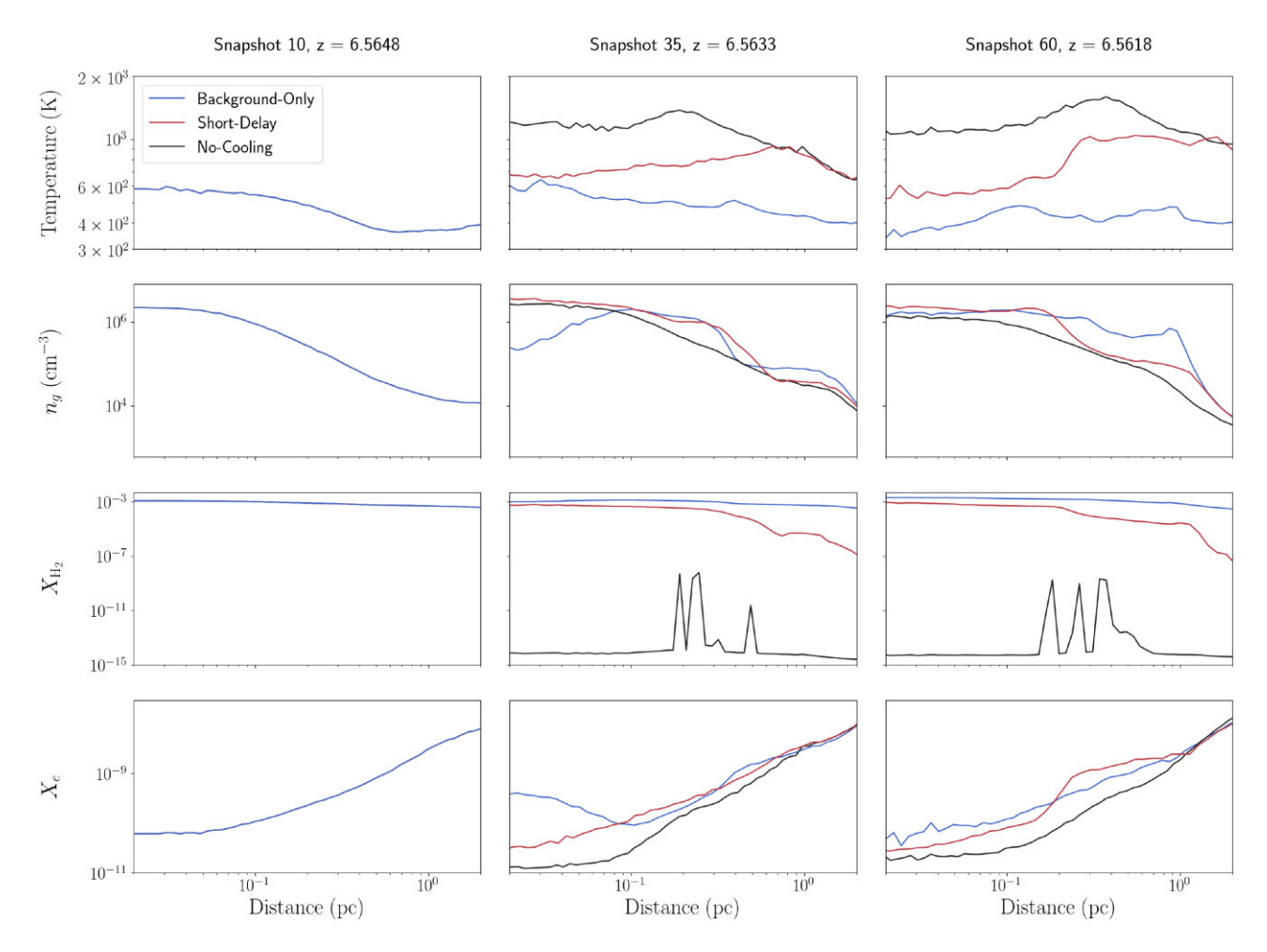


Figure 13. From top to bottom: radial profiles of temperature, gas number density, X_{H_2} , and electron density centred on sink A1. We display the region from 0.02 to 2 pc around sink A1. This limits the number of empty cells that the produce vertical spikes seen in the leftmost column. From left to right, the panels display the profiles at snapshot #10 (z = 6.5648), 2.5×10^5 yr later at snapshot #35 (z = 6.5633), and an additional 2.5×10^5 yr later at snapshot #60 (z = 6.5618). The lines again show the background-only, short-delay, and no-cooling runs. We see similar trends in the short-delay run compared to the bottom clump (Fig. 7). The additional LW drives an increase in temperature over the entire 2 pc region. It also drives a small region of increased density near sink A1. However, the density decreases outside of this \sim 0.1 pc core for the two runs with extra LW compared to the background-only run. In the short-delay run, X_{H_2} remains high in the high-density region around the sink particles before falling off at larger distances. X_{H_2} is significantly reduced across the entire region in the no-cooling run. The trend in X_e roughly mirrors that of the gas density, X_e decreases close to the sink particle but is raised in portions of the clump at larger r.

surrounding the accretion of significant amounts of hot, atomic gas on to an existing star.

4.4 Clump A

We now briefly describe the additional LW background's analogous effects on clump A and its protostar. We restrict our analysis in this section to the background-only and short-delay runs due to the similarities between clumps A and B. Its most massive sink particle, sink A1, forms in snapshot #11. This is in the middle of the additional LW flux increase in the short-delay run and prior to the additional LW flux being added in the long-delay run. We do not expect a massive star to form here, since the initial delay in accretion due to heating the gas will cause the existing protostar to collapse on to the main sequence at lower masses. However, we treat it as a second test site for studying how LW radiation affects the gas chemistry and cooling. We first discuss the LW background's effects on stellar growth and then the effects on nearby gas properties such as density, temperature, and $X_{\rm H_2}$.

As expected from clump B, introducing the short-delay LW radiation reduces the accretion rate and final mass of sink A1 (Fig. 12). This drop-off in both quantities is less drastic than sink B1's, whose accretion rate drops to zero. However, a notable difference is that clump A begins its collapse and forms a protostar prior to the LW background being added. It also has a higher gas density than clump B (see Figs 7 and 13). This prevents sink A1's accretion rate from dropping all the way to zero. However, the same trends of decreases in the accretion rate and the final sink mass are observed. The additional LW flux prevents the protostar from becoming a massive star.

Similarly to in clump B, the average temperature (measured again within 1 pc of the sink) increases in the presence of the added LW flux while the density initially decreases (background-only versus short-delay curves, Fig. 14). The clump's average temperature stalls well below the atomic cooling threshold of $\sim\!10^4\,\rm K$, preventing the gas from experiencing the desired isothermal collapse at higher temperatures. We therefore just increase the thermal energy of the gas, slowing accretion on to the protostar.

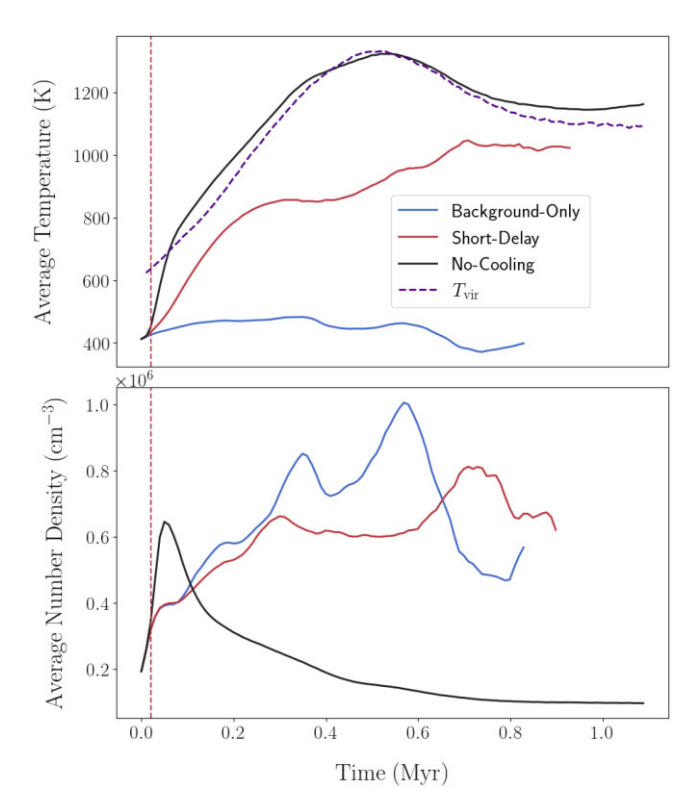


Figure 14. The top and bottom panels show the time evolution of the average temperature and density, respectively, within 1 pc of sink A1. Again the solid lines represent the background only, short-delay, and no-cooling runs, as in Fig. 12. The average gas virial temperature in the no-cooling run is traced by a dashed line. The vertical dashed line in both panels marks the time when the additional LW flux is added in the short-delay run. The average temperatures rise significantly immediately after the additional LW is introduced. However, the temperature does not reach the atomic cooling threshold at 10^4 K in either run. In the no-cooling run, it settles near the virial temperature, which flattens out at ~ 1200 K. The average number density in the short-delay run initially decreases with the additional LW flux but later surpass the background-only case at $\sim 6.5 \times 10^5$ yr. The number density initially spikes in the no-cooling run but decreases significantly after. This helps shut off accretion on to the sink particle (Fig. 12).

We again show profiles of the spherically-averaged temperature, density, $X_{\rm H_2}$, and $X_{\rm e}$ surrounding sink A1 at three different times (Fig. 13). The 1D profiles at snapshot #17 are replaced by snapshot #10 (the start of our simulation). The snapshot #10 profile is centred on clump A's maximum gas density, where sink A1 forms by the next snapshot.

We see the same general trends as in clump B with a couple of notable differences. The additional LW flux drives the temperature upwards more clearly, increasing it by nearly a factor of two at certain radii (Fig. 13). The density increases at the core of the clump when LW is added. However, this does not hold across the entire region. The background-only run contains higher density gas at certain radii. The $X_{\rm e}$ trend again roughly mirrors the gas number density and is similar to clump B's $X_{\rm e}$ profile.

The H_2 profiles again demonstrate the key reason why we do not see an increase in the accretion rates, while also showing the effect of a higher gas density. X_{H_2} drops off at larger radii when the LW turns on while the central region maintains its high X_{H_2} (Fig. 13). These radii where we see the drop-off are pushed out farther in comparison to clump B. This can be attributed to the higher density in this clump, which therefore retains a larger H_2 core. The LW fluxes we use are

clearly unable to dissociate the hydrogen at the high densities we reach at the centres of both clumps. The gas here is still able to cool via H_2 .

We further diagnose the internal LW flux's effect on clump A in Figs 15–17. These figures again display a projection of clump density, slice of temperature, and slice of $X_{\rm H_2}$, now centred on clump A/sink A1. It displays these for snapshots #10 (top row) and #60 (bottom row) in the initial three runs.

4.5 H₂ cooling removed

The above results, particularly the sub-critical accretion rates lasting longer than the Kelvin–Helmholtz contraction time, establish that we expect the sink particles to join the main sequence at low masses. However, a key finding is the high $X_{\rm H_2}$ at the centre of both clumps, which drives molecular cooling. The gas farther outside the clump cores begins to heat but it is uncertain whether this gas will be able to reach the atomic cooling threshold.

We introduce a final run, named 'no-cooling', to investigate what happens if we can dissociate the H₂ across the entire region containing the two clumps. This run is meant to be a thought experiment, choosing an artificially high LW flux to ensure we remove molecular cooling entirely. This seeks to answer whether the surrounding gas can warm up to the atomic-cooling limit and then collapse on to the sink particle before it joins the main sequence.

With this run, we can conclusively determine whether massive star formation is possible in our halo when H_2 cooling is removed. For simplicity, we add a constant $10^{10} \, \mathrm{J}_{21}$ internal LW flux beginning at dynamic collapse (z = 6.5618). This reduces X_{H_2} below 10^{-13} . Sink A1 is able to form because we add this additional flux just prior to its formation. However, we shut off cooling before sink B1 is able to form. We therefore focus our analysis on clump A and the only sink particle to form, sink A1.

Shutting off cooling drastically impacts sink A1's evolution. The accretion rate peaks at $9.53 \times 10^{-4}\,M_\odot\,yr^{-1}$ and then drops to zero by $5 \times 10^4\,yr$ (Fig. 12). This yields a final mass of $23.1\,M_\odot$. This reduced sink mass and the absence of additional sink particle formation clearly demonstrates that the high LW flux has suppressed both cooling and further collapse within the two protostellar cores.

We again plot the average temperature and density within a 1 pc sphere centred on the sink particle location (Fig. 14). The average temperature increases to 1300 K and then flattens out closer to 1200 K. These values are both higher than in any of the previous runs. The average gas density also initially spikes and then falls well below the corresponding gas densities in the background-only and short-delay runs. The higher LW flux produces a region of high temperature, more diffuse pressure-supported gas that no longer cools and collapses on to the sink particle.

We show phase diagrams of the gas temperature, density, and $X_{\rm H_2}$ to further reinforce these points (Fig. 18). At t=0, almost all the gas is below 1000 K. There is a wider range of densities $(5\times 10^{-22}~{\rm g\,cm^{-3}}\lesssim \rho\lesssim 5\times 10^{-18}~{\rm g\,cm^{-3}})$. The higher density gas has correspondingly higher $X_{\rm H_2}~(\sim 10^{-3})$ and the lower density gas has a lower value $(\sim 10^{-5})$. $X_{\rm H_2}$ quickly drops by roughly 10 orders of magnitude after the internal LW flux is turned on. The temperature experiences a corresponding increase while still retaining a wide spread in value ($t=2.5\times 10^5~{\rm yr}$, Fig. 18). This spread decreases with time, centring about the elevated average temperature. Apart from the initial spread in the range of temperatures, the phase space generally shrinks with time. The gas clump becomes increasingly uniform, centred around the average temperature and density displayed in Fig. 14. The top row of Fig. 18 displays the dynamical

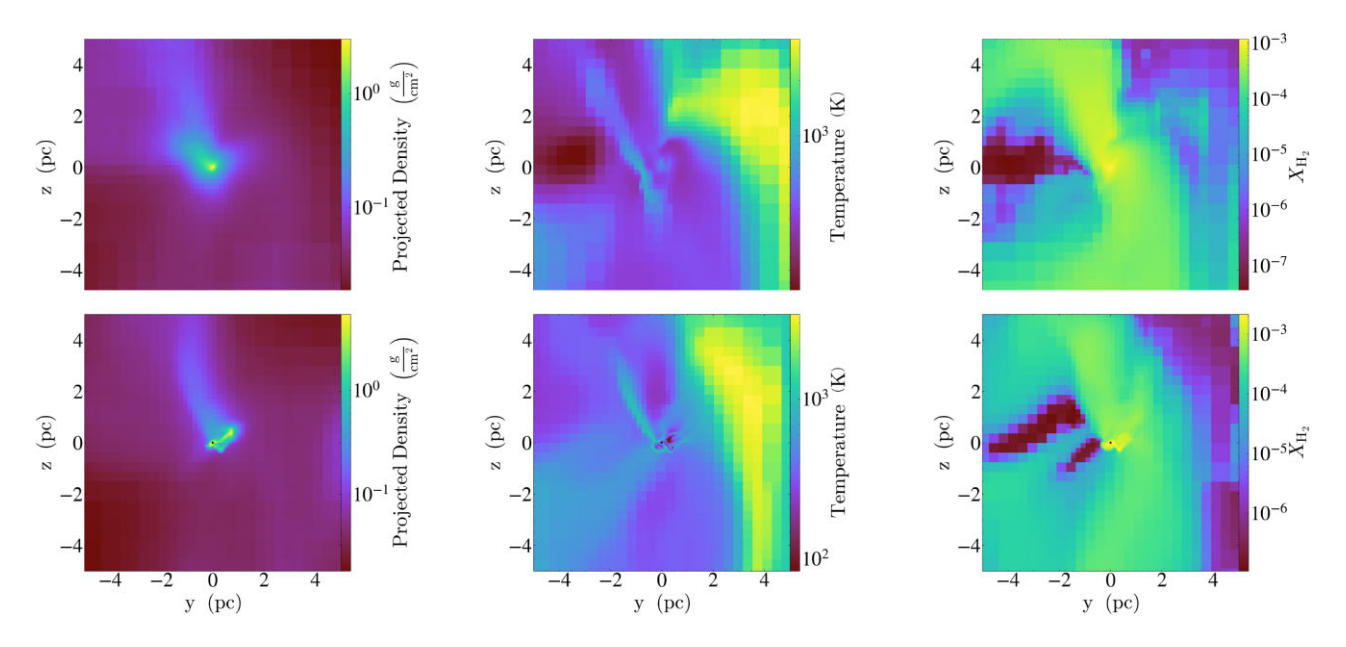


Figure 15. Same as Fig. 8 except centred about sink A1 and clump A. The top row now shows frames from snapshot #10, the simulation (re)start, centred about clump A's maximum density. The bottom row again displays these values at snapshot #60, centred about sink A1.

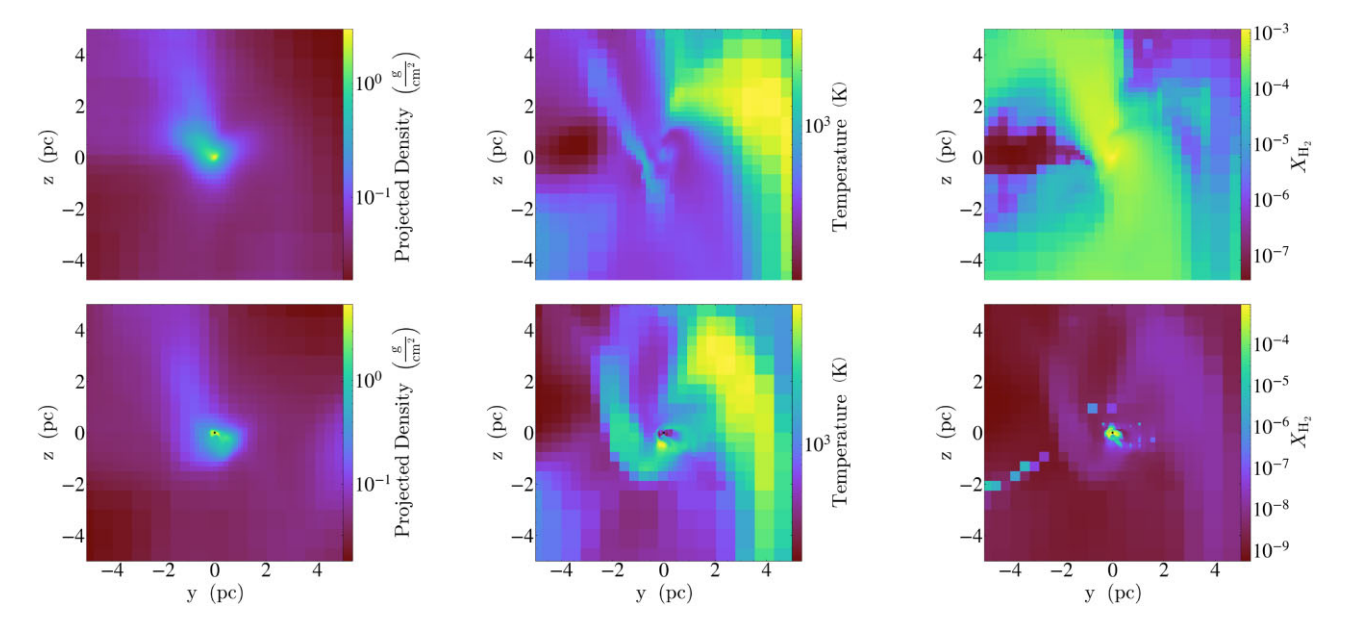


Figure 16. Same as Fig. 15 but for the short-delay run.

heating of the gas. The H_2 is removed and the gas has begun to heat. However, the bottom row displays that this gas reaches thermal equilibrium below the atomic cooling threshold. We conclude that a massive star does not form even in this extreme scenario.

We plot the halo virial temperature versus the radial distance from sink A1 to confirm the gas will not sufficiently heat to form a SMS. We define the virial temperature as $T_{\rm vir} = \frac{1}{3} \frac{GM \mu m_{\rm p}}{k_{\rm B} r}$, where M is the mass enclosed within radius r, μ is the mean molecular weight, and $m_{\rm p}$ is the mass of proton. The potential energy per unit mass at radius r is $-\frac{GM}{r}$, and the thermal energy per particle is $\frac{3}{2}k_{\rm B}T$. This gives us the factor 1/3. The LW radiation produces an increase in this virial temperature at low r, where the gas density dominates over DM in setting the virial temperature. However, it only manages to raise the virial temperature to ~ 1300 K. This agrees with the increase in

temperature displayed in Fig. 14. Additionally, we find that $T_{\rm gas} \sim T_{\rm vir}$ (Fig. 14), meaning that the gas has settled into quasi-hydrostatic equilibrium at this relatively low temperature. The gas will remain in this quasi-hydrostatic equilibrium until higher temperature gas at large radii begins falling into the halo centre. However, the virial temperature does not approach the atomic cooling threshold until as far away as $r \gtrsim 100$ pc. This is in part due to the halo's shallow DM profile. The gas's contribution to the virial temperature outweighs the DM's out to ~ 50 pc. The dynamical time, again approximated as $\frac{1}{\sqrt{4\pi}G\rho}$, for the gas near the atomic cooling threshold at $T \simeq 8000$ K (Fig. 19) is $\sim 5 \times 10^7$ yr. Similarly to in the previous runs, any protostar will contract and join the main sequence due to the sustained periods of low accretion well before this high-temperature gas can collapse in the central regions. Removing H₂ is still a necessary

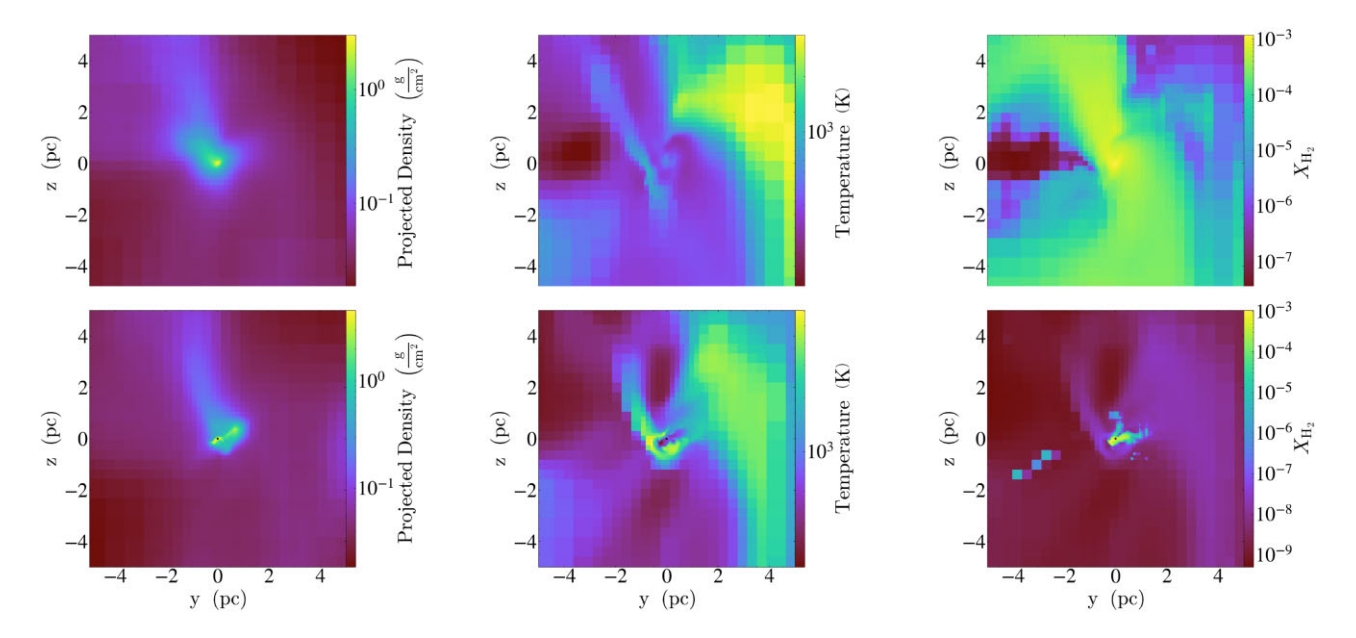


Figure 17. Same as Figs 15 and 16 but for the long-delay run.

condition for forming a SMS in this scenario but is insufficient on its own. It is foremost necessary to maintain a high protostar accretion rate.

4.6 Comparison to previous work

We do note the potential to still form SMSs through other 'internal' LW scenarios. Kiyuna, Hosokawa & Chon (2024) investigated a similar scenario in which a standard Pop III star formed within an ACH. In this halo, radiation from the first star prevents further star formation until the onset of cold accretion flows. This cold accretion, coupled with radiative feedback from the stars, enables the formation of SMSs fed by a disc of primarily atomic gas. In our set-up, we do not continue the simulation to see if cold flows will appear later on. This is due to the fact that our initial protostars maintain significantly lower accretion rates and will join the main sequence. Their stellar lifetimes are much shorter than the time-scale for cold accretion to kick in and so we would need to the consider potential metal pollution within the halo.

Dunn et al. (2018) also investigated internal LW feedback in a halo with multiple star-forming cores. They included the effect of internal LW radiation from star formation on massive direct collapse BH seeds in a cosmological simulation with GASOLINE. They found that the dominant LW sources producing massive BHs often resided a few 100 pc away in the same halo. However, their spatial resolution (few $\times\,10^{4-5}~M_{\odot}$ or few 100 pc) did not allow resolving the internal structure or the collapse of protostellar cores in haloes.

Similarly, Bhowmick et al. (2022) looked at massive star-forming haloes that contained pockets of pristine, dense gas. They studied the effect of varying the critical LW flux on BH seeding in these pockets, finding that increasing $J_{\rm crit}$ pushes seed formation to more massive haloes with increased star formation. Again, the resolution is beyond being able to resolve the formation and evolution of individual stars.

Our model more closely resembles Visbal et al. (2014)'s synchronized haloes scenario, even though they do not include an 'internal' LW flux. They instead consider two ACHs in close proximity. The first halo forms a galaxy right as the second begins to atomically cool. The galaxy then provides enough LW radiation to remove H₂

cooling in the second halo and enable DCBH formation. This avoids the potential metal enrichment of the second halo by supplying the LW flux from a separate, yet close, halo. The gas is also already at the atomic cooling threshold, avoiding two major issues we face in our scenario.

While our scenario does not support SMS star formation, the potential for forming a SMS star under slightly different conditions, such as those probed by Kiyuna et al. (2024), is promising for supplying additional routes for forming massive BH seeds in atomic cooling haloes. This, combined with other SMS formation routes such as Dunn et al. (2018) and Bhowmick et al. (2022)'s, supports the massive seed pathway for forming SMBHs.

5 CONCLUSIONS

We ran a set of hydrodynamic simulations using ENZO on an ACH with two collapsing protostellar clouds. We added a large 'internal' LW flux to model the protostellar feedback from the first protostar to form. We then measured the effects of this 'internal' LW flux on the final protostellar masses and their local environment. We first determined that the expected LW flux from the first protostar is too weak to dissociate H_2 around the second protostellar clump. This prevents the second protostar from forming through the collapse of warm, atomic hydrogen, instead producing a 'normal' mass Pop III star through molecular cooling. Most significantly, we then demonstrated that the second protostellar clump will not produce a massive star even if the H_2 is fully dissociated.

The first result was determined through the background-only, short-delay, and long-delay runs (Sections 4.2–4.4). The additional LW flux produced a decrease in the accretion rates and final masses of the most massive protostars in each clump. In clump A, the final mass decreased from $7000\,M_\odot$ (background only) to $6000\,M_\odot$ for the long-delay and $4600\,M_\odot$ for the short-delay run. In clump B, the maximum mass measured decreased from $2000\,M_\odot$ (background only) to $1000\,M_\odot$ for the long-delay and $250\,M_\odot$ for the short-delay run. In each case, the accretion rates are below the critical accretion rate to avoid joining the main sequence. In clump A, this is due to the regions of increased temperature and

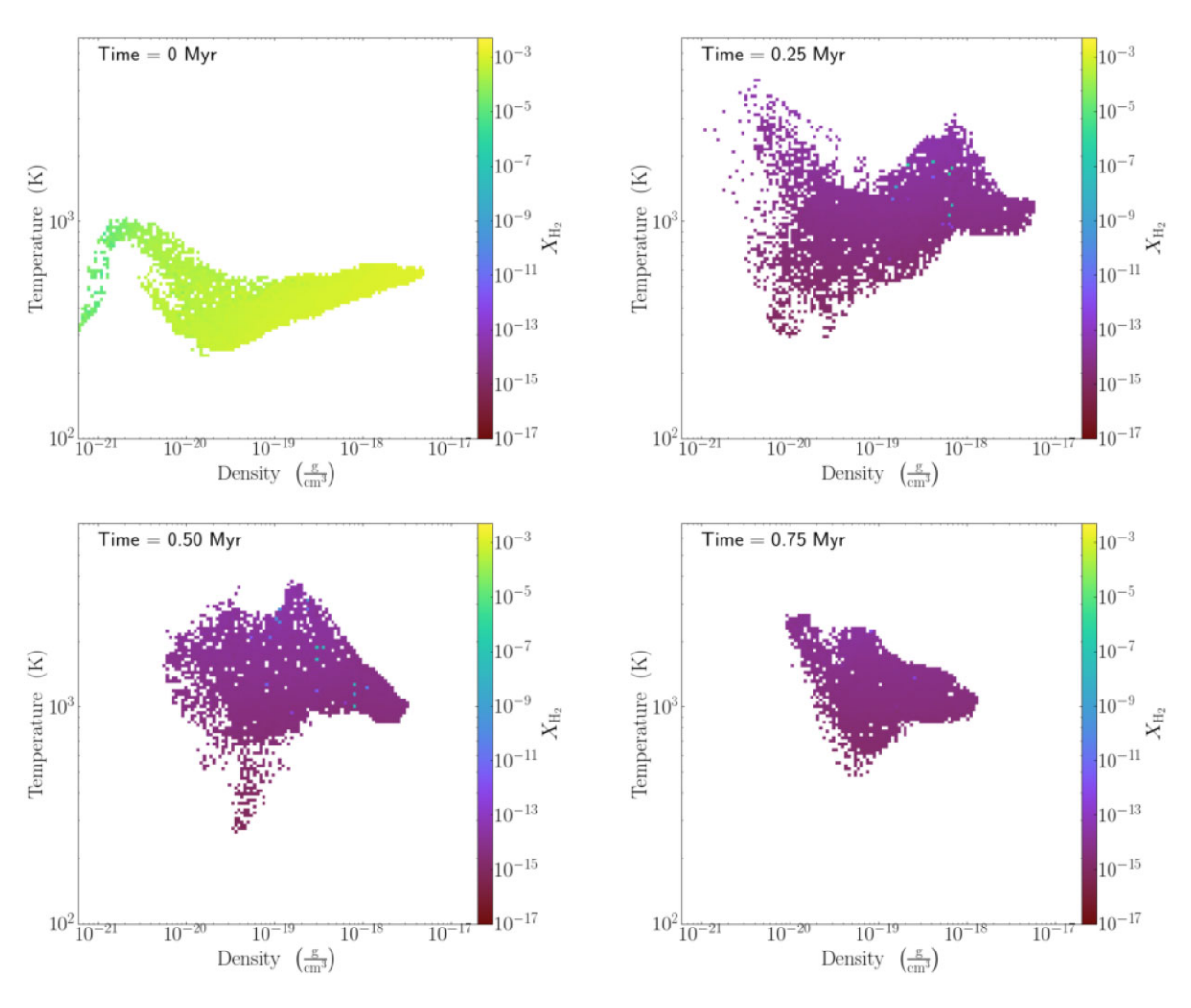


Figure 18. Phase diagrams of temperature, density, and $X_{\rm H_2}$ surrounding sink A1 at t=0 yr (top left), 2.5×10^5 yr (top right), 5.0×10^5 yr (bottom left), and 7.5×10^5 yr (bottom right) in the no-cooling run. Each panel shows gas within 1 pc from sink A1. We see the gas temperature rises when the LW flux is added. This corresponds with $X_{\rm H_2}$ dropping ~ 10 orders of magnitude. The spread of temperatures decreases after the initial burst in heating, producing a more uniform high-temperature region. The gas clump also becomes more uniform in density. We see that the gas cloud heats up before settling into isothermal, quasi-static equilibrium at a temperature around 10^3 K, well below the atomic-cooling threshold.

decreased density around the sink particles. In clump B, we see the same trend, albeit with a higher central density at certain times.

We found that even with H₂ fully dissociated in the no-cooling run (Section 4.5), the gas would not dynamically heat to the atomic cooling threshold before the first protostar joins the main sequence. Instead, the gas became pressure supported, settling at a temperature of ~1200 K. This internal LW flux from sequential star formation can therefore not produce a massive star in either gas cloud. Even if H₂ is fully dissociated, there is not sufficient time for the gas to heat to the atomic cooling threshold. In the typical massive Pop III star formation route, this heating is driven by gas falling in from the virial radius. The large potential energy at the edges of the DM halo is converted into thermal energy as the gas falls in. The gas in our halo has already undergone this dynamical collapse and is no longer able to rely on it to heat itself. It instead settles into a quasi-static thermal equilibrium at \sim 1300 K, demonstrated by the similar gas and virial temperatures at small radii (Fig. 14). It would require waiting $\sim 5 \times 10^7$ yr for gas near the atomic-cooling threshold at ~ 100 pc (Fig. 19), to collapse. The Kelvin-Helmholtz contraction time is orders of magnitude shorter (Section 4.3). The first protostar will

therefore settle on to the main sequence long before the surrounding gas heats to the atomic cooling threshold. This makes it unlikely we will form a SMS within the second protostellar core.

We therefore find that our halo lacks two necessary conditions for forming a massive protostar. The primary condition we lack is a sustained, high protostar accretion rate. We show there is a large unstable gas cloud available to fuel SMS formation (Fig. 3). However, the dynamical time for this gas is greater than 10⁵ yr, even with H₂ dissociated. This shut off accretion on to sink A1 and prevented additional sink particles, including sink B1, from forming. We need to decrease the dynamical time below this threshold in order to maintain protostellar accretion rates $\gtrsim 0.01-0.04 \,\mathrm{M}_\odot \,\mathrm{yr}^{-1}$. Again, periods of lower accretion lasting $\gtrsim 10^5$ yr produce a lower mass Pop III star. This requires a deeper potential well or some other source to drive gas towards the clump centre. This necessary deeper potential well limits the scenario to more unique haloes/regions. The second necessary condition, assuming higher protostellar accretion as discussed above, is a higher LW flux. We show that the LW flux is insufficient to dissociate the H₂ within the protostellar cores (Figs 7 and 13). The presence of H₂ will prevent atomic cooling close to the sink particle. This will stop inflowing gas from cooling

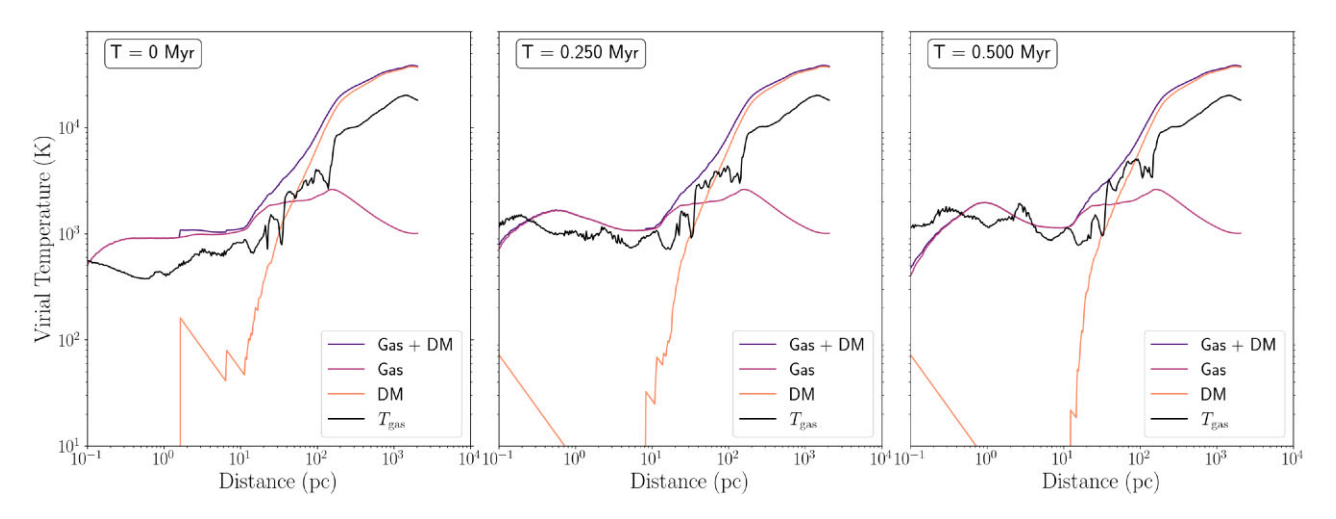


Figure 19. Radial profile of the virial temperature, centred around sink A1 in the no-cooling run. From left to right, the three panels show the profiles at snapshot #10 (z = 6.5648), 2.5×10^5 yr later at snapshot #35 (z = 6.5633), and an additional 2.5×10^5 yr later at snapshot #60 (z = 6.5618). The gas and DM-only contributions to the virial temperature are shown alongside the actual virial temperature to display which component dominates at different radii. This demonstrates that the LW flux does not increase the virial temperature up to the atomic cooling threshold at small radii. The $T \simeq 10^4$ K gas at ~ 100 pc has a dynamical time $t_{\rm dyn} \simeq 5 \times 10^7$ yr. It will not fall into the central clump in time to feed massive star formation.

and collapsing isothermally, leading to fragmentation and preventing SMS formation. This could be resolved in haloes with cores forming closer together, additional cores forming in quick succession, or a more massive first protostar. Each scenario would boost the 'internal' LW flux, increasing the H₂ survival density (dissociating the H₂ in the higher density clump centres). For example, moving the haloes to a distance $\sim\!5.78$ pc apart increases the H₂ survival density to $n_{\rm H}\cong6.0\times10^6$ cm $^{-3}$, surpassing the higher density regions of each clump. This would correspond to a new LW flux an order of magnitude larger ($\sim\!1.3\times10^5$ J₂₁). The likelihood of scenarios such as forming clumps at much closer distances would need to be assessed. Both of these conditions makes our neighbouring emission scenario unlikely to produce a large number of the massive BH seeds that later become SMBHs.

We expect these results to hold even more true for the more typical ACH population. As mentioned in Section 2, we analysed an ACH that forms later and is more massive than 'typical' ACHs, because its collapse was delayed by ionizing UV radiation. However, if anything, we expect these differences to make SMS formation easier. A large halo should have a deeper overall potential well, potentially increasing the gas accretion rate into the halo core. On the other hand, we do not expect a strong redshift dependence of the inner halo's potential. One concern could be that a higher ionization degree would speed up the formation of H- and therefore increase the H₂ abundance. This would work against atomic cooling and thus SMS formation. However, we find that the electron and H₂ fractions within our halo (Figs 7 and 13) are not raised in relation to a standard ACH (see fig. 4, Shang et al. 2010). We therefore regard our result as conservative, and expect our conclusions to hold for higher redshift ACHs.

Ultimately, we conclude that neighbouring protostellar cores do not help produce a massive star in either clump. However, they create a region of high-temperature gas around each of the protostellar cores. This could create a potential scenario in which a normal Pop III star forms within this well of relatively warm gas, which then undergoes rapid collapse at later times. The star may be unable to prevent the rapid collapse of this large r gas cloud tens of Myrs later. This scenario could be possible within massive ACHs with a single

star-forming core, driven by radiation from the first star itself, rather than a neighbouring one, and will be the subject of a follow-up study.

ACKNOWLEDGEMENTS

We thank the anonymous referee for comments that helped us improve the clarity of this manuscript. We acknowledge support from the United States National Science Foundation (NSF) grant AST-2006176 and the National Aeronautics and Space Administration (NASA) grants 80NSSC24K0440 and 80NSSC22K0822 (ZH). We also acknowledge support from NSF grant AST-2009309, NASA Astrophysics Theory Program grant 80NSSC22K0629, and Space Telescope Science Institute grant JWST-AR-05238 (EV). The simulations in this work were run on Texas Advanced Computing Center's Stampede2 and Stampede3 systems. We used Stampede2 and Purdue University's computing system Anvil for data analysis.

DATA AVAILABILITY

The underlying data will be shared upon reasonable request of the corresponding author.

REFERENCES

Abel T., Anninos P., Zhang Y., Norman M. L., 1997, New Astron., 2, 181

Abel T., Bryan G. L., Norman M. L., 2000, ApJ, 540, 39

Abel T., Bryan G. L., Norman M. L., 2002, Science, 295, 93

Ahn K., Shapiro P. R., Iliev I. T., Mellema G., Pen U.-L., 2009, ApJ, 695, 1430

Alvarez M. A., Wise J. H., Abel T., 2009, ApJ, 701, L133

Bañados E. et al., 2018, Nature, 553, 473

Becerra F., Greif T. H., Springel V., Hernquist L. E., 2014, MNRAS, 446, 2380

Begelman M. C., Rees M. J., 1978, MNRAS, 185, 847

Begelman M. C., Volonteri M., Rees M. J., 2006, MNRAS, 370, 289

Begelman M. C., Rossi E. M., Armitage P. J., 2008, MNRAS, 387, 1649

Berger M. J., Colella P., 1989, J. Comput. Phys., 82, 64

Bhowmick A. K., Blecha L., Torrey P., Kelley L. Z., Vogelsberger M., Nelson D., Weinberger R., Hernquist L., 2022, MNRAS, 510, 177

838 J. Sullivan et al. Bosman S., 2024, All z > 5.7 quasars currently known, Zenodo, Version 2.2.1, https://doi.org/10.5281/zenodo.13170305(accessed December 09). Bromm V., 2013, Rep. Prog. Phys., 76, 112901 Bromm V., Loeb A., 2003, ApJ, 596, 34 Bromm V., Yoshida N., 2011, ARA&A, 49, 373 Bromm V., Coppi P. S., Larson R. B., 2002, ApJ, 564, 23 Bryan G. L., Norman M. L., 1997, preprint(astro-ph/9710187) Bryan G. L. et al., 2014, ApJS, 211, 19 Chon S., Latif M. A., 2017, MNRAS, 467, 4293 Devecchi B., Volonteri M., 2009, ApJ, 694, 302 Dijkstra M., Haiman Z., Mesinger A., Wyithe J. S. B., 2008, MNRAS, 391, 1961 Dunn G., Bellovary J., Holley-Bockelmann K., Christensen C., Quinn T., 2018, ApJ, 861, 39 Fan X. et al., 2006, AJ, 131, 1203 Fan X., Bañados E., Simcoe R. A., 2023, ARA&A, 61, 373 Feathers C. R., Visbal E., Kulkarni M., Hazlett R., 2024, ApJ, 962, 62 Galli D., Palla F., 1998, A&A, 335, 403 González E., Kremer K., Chatterjee S., Fragione G., Rodriguez C. L., Weatherford N. C., Ye C. S., Rasio F. A., 2021, ApJ, 908, L29 Greif T. H., 2015, Comput. Astrophys. Cosmol., 2, 3 Greif T. H., Bromm V., Clark P. C., Glover S. C. O., Smith R. J., Klessen R. S., Yoshida N., Springel V., 2012, in Umemura M., Omukai K., eds, AIP Conf. Proc. Vol. 1480, First Stars IV – From Hayashi to the Future. Am. Inst. Phys., New York, p. 51 Haemmerlé L., Woods T. E., Klessen R. S., Heger A., Whalen D. J., 2018, MNRAS, 474, 2757 Haiman Z., Loeb A., 1997, ApJ, 483, 21 Haiman Z., Thoul A. A., Loeb A., 1996, ApJ, 464, 523 Haiman Z., Abel T., Rees M. J., 2000, ApJ, 534, 11 Heger A., Fryer C. L., Woosley S. E., Langer N., Hartmann D. H., 2003, ApJ, Hirano S., Bromm V., 2017, MNRAS, 470, 898 Hirano S., Hosokawa T., Yoshida N., Umeda H., Omukai K., Chiaki G., Yorke H. W., 2014, ApJ, 781, 60 Hosokawa T., Omukai K., Yorke H. W., 2012, ApJ, 756, 93 Hosokawa T., Yorke H. W., Inayoshi K., Omukai K., Yoshida N., 2013, ApJ, Inayoshi K., Visbal E., Haiman Z., 2020, ARA&A, 58, 27 Katz H., Sijacki D., Haehnelt M. G., 2015, MNRAS, 451, 2352 Kiyuna M., Hosokawa T., Chon S., 2024, MNRAS, 534, 3916 Klessen R., 2019, in Latif M., Schleicher D., eds, Formation of the First Black Holes. World Scientific Publishing Co. Pte. Ltd., Singapore,p. 67–97. Klessen R. S., Glover S. C. O., 2023, ARA&A, 61, 65 Kormendy J., Ho L. C., 2013, ARA&A, 51, 511 Krumholz M. R., McKee C. F., Klein R. I., 2004, ApJ, 611, 399

Kulkarni M., Visbal E., Bryan G. L., 2019, ApJ, 882, 178 Kulkarni M., Visbal E., Bryan G. L., 2021, ApJ, 917, 40

Machacek M. E., Bryan G. L., Abel T., 2001, ApJ, 548, 509

Milosavljević M., Couch S. M., Bromm V., 2009, ApJ, 696, L146 Nandal D., Regan J. A., Woods T. E., Farrell E., Ekström S., Meynet G., 2023,

McGreer I. D., Bryan G. L., 2008, ApJ, 685, 8

A&A, 677, A155

Latif M. A., Schleicher D. R. G., Hartwig T., 2016, MNRAS, 458, 233

```
O'Shea B. W., Bryan G., Bordner J., Norman M. L., Abel T., Harkness R.,
    Kritsuk A., 2004, preprint(astro-ph/0403044)
Omukai K., 2001, ApJ, 546, 635
Omukai K., Schneider R., Haiman Z., 2008, ApJ, 686, 801
Planck Collaboration XVI, 2014, A&A, 571, A16
Portegies Zwart S. F., Baumgardt H., Hut P., Makino J., McMillan S. L. W.,
    2004, Nature, 428, 724
Prieto J., Jimenez R., Haiman Z., 2013, MNRAS, 436, 2301
Rahmati A., Pawlik A. H., Raičević M., Schaye J., 2013, MNRAS, 430, 2427
Rees M. J., 1978, Phys. Scr, 17, 193
Regan J. A., Downes T. P., 2018, MNRAS, 478, 5037
Regan J. A., Haehnelt M. G., 2009a, MNRAS, 393, 858
Regan J. A., Haehnelt M. G., 2009b, MNRAS, 396, 343
Regan J. A., Visbal E., Wise J. H., Haiman Z., Johansson P. H., Bryan G. L.,
   2017, Nat. Astron., 1, 0075
Regan J. A., Wise J. H., O'Shea B. W., Norman M. L., 2020, MNRAS, 492,
   3021
Rizzuto F. P. et al., 2021, MNRAS, 501, 5257
Sakurai Y., Vorobyov E. I., Hosokawa T., Yoshida N., Omukai K., Yorke H.
   W., 2016, MNRAS, 459, 1137
Shang C., Bryan G. L., Haiman Z., 2010, MNRAS, 402, 1249
Smith B. D., Regan J. A., Downes T. P., Norman M. L., O'Shea B. W., Wise
   J. H., 2018, MNRAS, 480, 3762
Spinoso D., Bonoli S., Valiante R., Schneider R., Izquierdo-Villalba D., 2022,
   MNRAS, 518, 4672
Stacy A., 2012, American Astronomical Society Meeting Abstracts #219. p.
Stacy A., Greif T. H., Bromm V., 2010, MNRAS, 403, 45
Sugimura K., Omukai K., Inoue A. K., 2014, MNRAS, 445, 544
Tegmark M., Silk J., Rees M. J., Blanchard A., Abel T., Palla F., 1997, ApJ,
   474.1
Venemans B. P. et al., 2015, ApJ, 801, L11
Visbal E., Haiman Z., Bryan G. L., 2014, MNRAS, 445, 1056
Visbal E., Bryan G. L., Haiman Z., 2017, MNRAS, 469, 1456
Volonteri M., Habouzit M., Colpi M., 2021, Nat. Rev. Phys., 3, 732
Wang F. et al., 2021, ApJ, 907, L1
Wise J. H., Abel T., 2007, ApJ, 671, 1559
Wise J. H., Turk M. J., Abel T., 2008, ApJ, 682, 745
Wolcott-Green J., Haiman Z., 2019, MNRAS, 484, 2467
Wolcott-Green J., Haiman Z., Bryan G. L., 2011, MNRAS, 418, 838
Wolcott-Green J., Haiman Z., Bryan G. L., 2017, MNRAS, 469, 3329
Woods T. E., Heger A., Whalen D. J., Haemmerlé L., Klessen R. S., 2017,
   ApJ, 842, L6
Woods T. E. et al., 2019, Publ. Astron. Soc. Aust., 36, e027
Wu X.-B. et al., 2015, Nature, 518, 512
Yoshida N., Abel T., Hernquist L., Sugiyama N., 2003, ApJ, 592, 645
Yoshida N., Hosokawa T., Omukai K., 2012, Prog. Theor. Exp. Phys., 2012,
   01A305
Zubovas K., King A., 2021, MNRAS, 501, 4289
This paper has been typeset from a TFX/IATFX file prepared by the author.
```

O'Shea B. W., Norman M. L., 2007, ApJ, 654, 66

O'Shea B. W., Norman M. L., 2008, ApJ, 673, 14